High-performance plasmas after pellet injections in Wendelstein 7-X

S.A. Bozhenkov[1], Y. Kazakov[2], O.P. Ford[1], M.N.A. Beurskens[1], J. Alcusón[1], J.A. Alonso[3], J. Baldzuhn[1], Ch. Brandt[1], K.J. Brunner[1], H. Damm[1], G. Fuchert[1], J. Geiger[1], O. Grulke[1], M. Hirsch[1], U. Höfel[1], Z. Huang[7], J. Knauer[1], M. Krychowiak[1], A. Langenberg[1], H.P. Laqua[1], S. Lazerson[1], N. B. Marushchenko[1], D. Moseev[1], M. Otte[1], N. Pablant[4], E. Pasch[1], A. Pavone[1], J.H.E. Proll[5], K. Rahbarnia[1], E.R. Scott[1], H.M. Smith[1], T. Stange[1], A. von Stechow[1], H. Thomsen[1], Yu. Turkin[1], G. Wurden[6], P. Xanthopoulos[1], D. Zhang[1], R.C. Wolf[1] and W7-X Team

[1] Max-Planck-Institut für Plasmaphysik, D-17491 Greifswald, Germany
[2] Laboratory for Plasma Physics, LPP-ERM/KMS, Brussels, Belgium
[3] Laboratorio Nacional de Fusión, CIEMAT, Madrid, Spain
[4] Princeton Plasma Physics Laboratory, Princeton, NJ, USA
[5] Eindhoven University of Technology, Eindhoven, The Netherlands
[6] Los Alamos National Laboratory, Los Alamos, NM, USA
[7] MIT Plasma Science and Fusion Center, Cambridge, USA

E-mail: `sergey.bozhenkov@ipp.mpg.de`

Abstract. A significant improvement of plasma parameters in the optimized stellarator W7-X is found after injections of frozen hydrogen pellets. The ion temperature in the post-pellet phase exceeds 3 keV with 5 MW of electron heating and the global energy confinement time surpasses the empirical ISS04-scaling. The plasma parameters realized in such experiments are significantly above those in comparable gas-fuelled discharges. In this paper, we present details of these pellet experiments and discuss the main plasma properties during the enhanced confinement phases. Local power balance is applied to show that the heat transport in post-pellet phases is close to the neoclassical level for the ion channel and is about a factor of two above that level for the combined losses. In comparable gas-fuelled discharges, the heat transport is by about ten times larger than the neoclassical level, and thus is largely anomalous. It is further observed that the improvement in the transport is related to the peaked density profiles that lead to a stabilization of the ion-scale turbulence.

1. Introduction

In recent Wendelstein 7-X (W7-X) experiments, injection of a series of hydrogen pellets was successfully applied for core plasma fuelling [1]. This allowed one to raise the central electron density above 10^{20} m^{-3} and often resulted in transient post-pellet phases with enhanced performance, as observed in the plasma pressure, global energy confinement time and, most prominently, in the ion temperature. The energy confinement time in these post-pellet plasmas exceeds the empirical stellarator scaling ISS04 [2] and at the same time the ion temperature reaches values above 3 keV with an input heating power of 5 MW to the electrons. The combination of the improved confinement and of the high ion temperature implies a high triple product, as reported previously [3]. Plasma pressure effects, Shafranov shift and finite-β shift of the ECRH deposition, become noticeable [4]. Gas fuelled discharges at similar densities and heating powers show a significantly lower performance. The difference between the two types of discharges seems to be caused by a strong reduction of the anomalous heat transport. In this paper, we present details of the pellet experiments tailored for improved plasma parameters and discuss results of a transport analysis of such discharges.

Enhanced performance in pellet fuelled plasmas is not unique for W7-X and was previously observed in many other devices [5]. In tokamak experiments, e.g. in JET [6–8], Tore Supra [9], DIII-D [10], ASDEX [11], Alcator C [6], such regimes are often called pellet enhanced performance. A similar phenomenon was found in the large heliotron experiment LHD [12, 13]. Generally, the improvement is attributed to a reduction in the ion loss channel in the plasma core, caused by the stabilization of ion temperature gradient (ITG) modes by the peaked density profiles, i.e. by sufficiently large density gradients [5, 14, 15]. The turbulence stabilization in tokamaks can be additionally supported by the formation of a central reversed shear region due to the bootstrap current at the location of the large density gradient [8]. It is worth mentioning that confinement improvements were observed in the past also in other cases with peaked density profiles [15–17]. In particular, an optimum confinement regime was developed in the preceding experiment W7-AS [17–20], where some similarities to post-pellet phases in W7-X can be noted: narrow density profiles, high ion temperatures and triple product, energy transport at the neoclassical level. Though, further studies are necessary to verify whether the same mechanism is responsible for the reduction of anomalous losses in both cases.

The present results from the low-shear stellarator W7-X enrich previous observations with a new set of well diagnosed discharges. They also give a new insight into the turbulence physics in optimized magnetic configurations, where, for example, trapped electron modes (TEM) are expected to be more stable [21, 22]. From an operational point of view, these discharges demonstrate the highest performance attained in W7-X so far and offer a way to assess effects of the W7-X optimization, e.g. the reduced Shafranov shift or the minimized neoclassical transport, even with the presently limited heating power. Experiments reported here were realized with electron heating by

ECRH, whereas NBI-heating is usually applied in other experiments.

Wendelstein 7-X [23] is a large optimized stellarator that aims to demonstrate steady state operation at β values up to 5% and ion temperatures up to 5 keV [24, 25], for which the neoclassical transport at low collisionalities was optimized via a reduction of the effective helical ripple. Operation at high ion temperatures and plasma pressures implies high plasma densities of up to $2 \cdot 10^{20}$ m^{-3}, because neoclassical transport coefficients scale beneficially with the density in the stellarator $1/\nu$ regime [26, 27] and also because of improved collisional power transfer between electrons and ions. Realization of high densities can be potentially complicated, at least in theory, by several factors. Firstly, the density profiles are predicted to become unstably hollow in neoclassically dominated plasmas with edge fuelling [20, 28]. Secondly, the employed island divertor configuration is expected to effectively screen the gas fuelling at such densities [29]. Besides, a separate method of core plasma fuelling is desired for controlling the density profile shape for transport studies. For all these reasons, hydrogen pellet injections were proposed as an option to both reliably access high densities and to generate a central density peaking.

The potential difficulties with edge fuelling did not turn out to be critical for the present W7-X operational conditions. In particular, the density profiles are observed to be flat instead of hollow, which may be related to the fact that neoclassical transport is not the dominant transport mechanism. In 2018, boronization [30] helped to raise the achievable central density up to $1.4 \cdot 10^{20}$ m^{-3}, i.e. the pronounced radiative density limit that scales roughly as a square root of the heating power [31] was significantly relaxed. Although, it has to be noted that pellet injections allow to decouple the edge and core densities; and therefore helped to reach such high densities even before the boronization. For example, a plasma operation above the X2-ECRH cut-off density of $1.2 \cdot 10^{20}$ m^{-3} was first demonstrated with the pellet injection [32] and O2-ECRH heating. More pertinently, it was found that injections of a series of hydrogen pellets can produce peaked density profiles, thereby improving the overall plasma performance. It is these latter scenarios that are considered in this paper.

In the recent experimental campaign OP1.2 that took place in 2017 and 2018 [30], a pellet injector with a restricted number of pellets [33] was available to verify the fuelling performance, to compare the outboard and inboard side injections and to test operational scenarios. In this paper, we study the properties of plasmas after pellet injections and compare them to similar gas-fuelled discharges. The physics of pellet penetration and fuelling is reported elsewhere [1].

The rest of the paper is organized in the following way: in section 2, W7-X experimental conditions and the main diagnostics are introduced; in section 3, details of the pellet experiments and plasma properties during enhanced phases are described; in section 4, a transport analysis of the phases with improved confinement is compared to that of gas-fuelled discharges with comparable parameters; and finally, in section 5, the results are summarized.

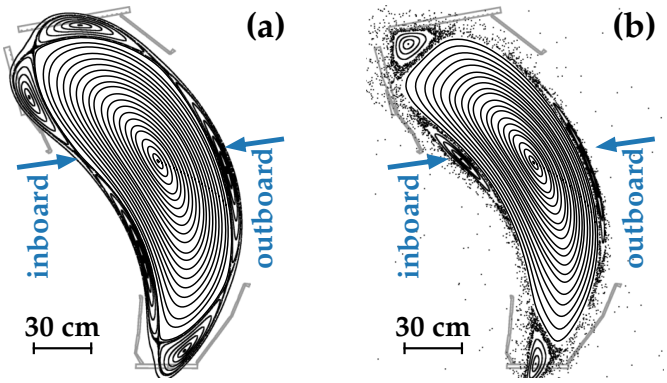

Figure 1: Plasma cross section at the location of the pellet injection system. (a) - standard configuration with five islands at the boundary; (b) - high-iota configuration with four edge islands and partially stochastic field lines around [34]. The black lines show a Poincaré plot of vacuum flux surfaces. Divertor and baffle plates are plotted in gray. The approximate directions of the pellet injection from the inboard and outboard sides are indicated in blue. The device center is on the left side.

2. Description of the experimental conditions

Wendelstein 7-X is a fivefold symmetric stellarator with an average major radius of 5.5 m, an effective minor radius of 0.5 m and a plasma volume of about 30 m^3. Its flux surfaces are produced entirely by external coil systems that include superconducting non-planar and planar coils. The former, originating from the W7-X optimization procedure [23,24,35–37], generate both the toroidal and poloidal field components, while the latter are used for fine adjustments of the horizontal position and of the rotational transform. There are five different types of non-planar coils and two types of planar coils, which provide a wide flexibility of possible magnetic configurations.

The magnetic configurations differ in the axis location, rotational transform, magnetic shear, effective helical ripple, toroidal mirror and island divertor structure. In the present work, only two configurations, namely "standard" and "high-iota", were used. In the standard case, the rotational transform grows from about 0.85 on the axis to 1.0 at the plasma boundary and the effective helical ripple ε_{eff} is around 0.9%. In the high-iota configuration, the rotational transform increases from about 1.01 on the axis to 1.25 at the plasma boundary and the effective helical ripple is around 1.5%. Further details of possible W7-X magnetic configurations can be found in [38, 39]. A more detailed description of the W7-X coil systems and profiles of the rotational transform can be found in [38–40].

The main heating method at W7-X is second harmonic, steady-state capable electron cyclotron resonance heating (ECRH) [4,32]. The ECRH system consists of 10 gyrotrons with the output frequency of 140 GHz and a combined power up to 7.5 MW launched into the plasma. It can be operated both in the extraordinary (X2) and in the ordinary

(O2) polarization. In theory, the X2-operation is restricted to plasma densities below the cut-off of $1.2 \cdot 10^{20}$ m^{-3}. In practice, the density should stay below about 10^{20} m^{-3} to prevent a too strong refraction and, as a consequence, an increased level of unabsorbed microwave stray radiation. The cut-off density for the O2-mode is $2.4 \cdot 10^{20}$ m^{-3} and the operational limit is about $1.8 \cdot 10^{20}$ m^{-3}. O2-operation requires sufficiently high values of the electron density and temperature for a tolerable single pass absorption, thus necessitating initial plasma start-up in the X2-mode and a switch to the full O2-polarization during the discharge [32]. Most experiments in this study were conducted with the X2-polarization, though some examples with the O2-polarization are available. The radial location of the X2 power deposition can be varied with front steerable mirrors for each beam and via the absolute value of the magnetic field. For example, an on-axis deposition is realized with the field strength of 2.52 T. The time dependant heating waveform can be prescribed with a large degree of flexibility, including power ramp-ups, ramp-downs and modulations.

In the second half of the OP1.2 campaign neutral beam injection (NBI) became available in addition to the ECRH [41, 42]. The NBI system consists of two sources with about 1.7 MW of power into the vessel each (H at 55 keV). In experiments analyzed in this paper it was used only for short "blips" with a pulse duration of 10 ms and repetition rate of 10 Hz, for charge exchange measurements of the ion temperature.

The power and particle exhaust in W7-X are handled with the help of an island divertor [43, 44]. In such configurations, divertor targets, arranged in ten equivalent divertor units, intersect an island chain at the plasma boundary. The area of intense plasma wall interaction is, thus, topologically separated from the core confinement region. The island divertor is predicted to provide sufficient power spreading for steady state operation with 10 MW input power and has been recently demonstrated to maintain stable heat flux detachment [45, 46]. The edge island structure, as well as the strike line position, varies with the magnetic configuration. In particular, the island structure is different for the two configurations used: in the standard case, the divertor is formed by a $m/n = 5/5$ island chain touching both the vertical and the horizontal target plates; whereas in the high-iota case the divertor geometry is created by a $m/n = 4/5$ island chain in contact only with the horizontal target, as can be seen in figure 1. The 5/5 island configuration is sensitive to 1/1 error fields [47]. Therefore, in this case an experimentally determined field correction [48, 49] was applied with the help of a special set of compensation coils, known as trim coils, to allow operation with the full heating power. In the campaign OP1.2, the divertor targets were inertially cooled, which limited the maximal injected energy. In the future, the divertor will be exchanged for a water-cooled one and the pulse duration will be gradually extended to 30 minutes [25].

The pellet injector that was available in the last experimental campaign is of blower gun type with the injection frequency variable between 5 and 30 Hz and the total number of pellets up to 40 [33]. The pellets are cylindrical, 2 mm in diameter and 2 mm in length, corresponding to about $3 \cdot 10^{20}$ atoms, and are injected with a speed of 250 m/s. The

injector is connected both to the outboard and inboard sides of the stellarator via 14.5 m and 29 m long guiding tubes respectively and for this work alternating injections of series of pellets from both sides were used. Pellets in such series can penetrate only as deep as 40% of the minor radius but, nonetheless, lead to peaked density profiles [1]. A further analysis of the pellet fuelling efficiency, its dependence on the plasma parameters, and a comparison of both injection sides can be found in the same reference. A schematic of the pellet injection geometry is given in figure 1 for the two configurations used in the paper.

The principal plasma parameters of W7-X are well diagnosed [50]. The main systems used throughout the paper are: a dispersion interferometer for the line integrated density [51]; a Thomson scattering system for the electron density and electron temperature profiles [52, 53]; an electron cyclotron emission (ECE) diagnostic with 32 channels for electron temperature profiles (calibrated with a cold source) [54, 55]; a multi-line X-ray imaging crystal spectrometer (XICS) for profiles of ion temperature and radial electric field [56, 57]; a charge exchange recombination spectroscopy (CXRS) diagnostic for profiles of ion temperature and radial electric field [58]; a compensated diamagnetic loop for the plasma energy [59]; and a gold foil multi-line bolometer system for total radiated power and plasma radiation power profiles [60]. In the first half of the campaign, the Thomson scattering diagnostic covered a half profile with 16 spatial points and ran with a repetition rate of 10 Hz. For the second half, the Thomson scattering system was improved to cover the full profile with 42 channels and to provide data with a repetition rate of 30 Hz. The measurement chord of the dispersion interferometer is almost identical to the laser line of the Thomson scattering system; consequently, the latter can be conveniently cross-calibrated. Ion temperature profiles can be recovered from the XICS measurements of Ar^{+16} line widths along multiple lines of sight by using either a tomographic inversion with the known flux surface geometry [61] or a Bayesian modelling with Minerva framework [62]. In addition, high quality carbon ion temperature profiles can be measured with the CXRS diagnostic on the NBI, where the number of spatial channels varies between 30 and 70, depending on the diagnostic settings.

To map data of the profile diagnostics to flux surfaces, coordinate transformations based on results of the equilibrium code VMEC [63] are applied in this work. At W7-X, VMEC is available as a web-service [64], together with a wide data base of precomputed equilibria. In particular, the VMEC data base includes equilibria for reference magnetic configurations with a vanishing plasma pressure, referred to as vacuum equilibria, which provide an adequate accuracy for plasmas at low parameters. In high performance cases, dedicated VMEC calculations are performed using experimentally measured pressure profiles, i.e. with the help of profile data from the Thomson scattering, XICS and CXRS systems. In these experiments, the toroidal plasma current is below 2 kA and can be neglected. The calculations are initiated with pressure profiles mapped with the closest available equilibrium and are iterated until convergence on the millimeter level is achieved between the resulting profile mapping and the input. The quality of this

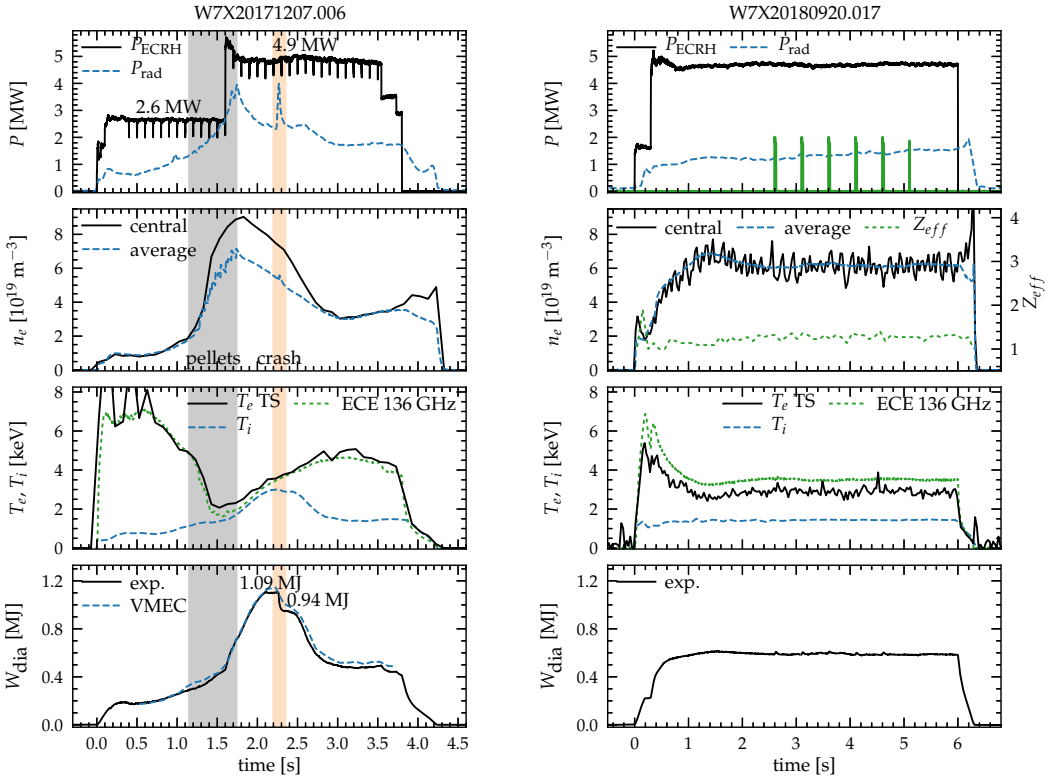

Figure 2: Comparison of a pellet discharge with enhanced confinement phase (left) and a discharge without pellet fuelling but with a comparable average density and heating power (right). The quantities shown from top to bottom are: the auxiliary heating and radiated power; the line averaged (interferometer), central densities (cross-calibrated Thomson scattering) and $Z_{\rm eff}$ from visible spectroscopy (for discharges after boronization); the central electron (ECE and Thomson scattering) and ion (XICS) temperatures; the diamagnetic (diamagnetic loop) and kinetic (VMEC equilibrium) plasma energies. Both discharges were performed in the standard magnetic configuration. The gray area in the left plots marks the pellet injection period. The orange area highlights an MHD event discussed later in the paper.

procedure is also confirmed by a good agreement of the calculated kinetic plasma energy to the measured diamagnetic energy, see figure 2. A further discussion of equilibrium reconstructions for W7-X can be found in [65].

3. Pellet experiments with enhanced confinement phases

Enhanced confinement phases in W7-X are realized by injecting a series of hydrogen pellets of a preset frequency and length into ECRH heated discharges. A prominent example of such an experiment, discharge *W7X20171207.006*, is illustrated on the left hand side of figure 2. The discharge is started at a low density of about 10^{19} m^{-3} and modest heating power of about 2.6 MW, as to allow a deeper pellet penetration

and, hence, to amplify the electron density peaking. The pellet series is initiated at a pre-programmed time around 1.1 s and the injection is performed from both sides to maximize the fuelling rate. The central pellet fuelling results in a significant density peaking, which can be readily seen from the difference between the line averaged and central density in the time window between 1.3 and 3 s. At the end of the pellet series at about 1.6 s the heating power is stepped up to 4.9 MW. The pellet phase is terminated at about 1.7 s and after that the density and the peaking decay, while temperatures recover quickly. There is a pronounced increase in the diamagnetic energy, i.e. an improvement in the energy confinement, in the post-pellet period. The improved confinement phase lasts from 1.8 s till 2.7 s, with the maximal parameters being achieved between 2 and 2.5 s. The peak value of the plasma stored energy is about 1.1 MJ corresponding to the volume averaged β of about 1%. In addition, a close equilibration of the ion and electron temperatures at the level of 3 keV is observed, whereas before and after this phase, electrons are usually much hotter than ions. The enhanced plasma parameters correspond to the highest triple product value achieved in W7-X [3].

The length of the pellet series in these experiments is chosen empirically to reach the maximum peak density compatible with heating in the X2-polarization. This maximal density of 10^{20} m^{-3} is realized with the injection of 10 to 20 pellets at 20 to 30 Hz, depending on the conditions of the first wall. It is also possible to raise the density above the X2 cut-off by operating the ECRH in the O2-polarization [32]. An example of a pellet injection experiment with the O2-ECRH heating, discharge *W7X20180911.033*, is shown on the right of figure 5 with a similar resulting improvement in confinement. In this case the maximal density possible for the given fuelling rate and used heating power was achieved. Given that no additional performance enhancement is found in the pellet experiments with the O2-heating, X2-experiments are preferred due to a more straightforward configuration of the ECRH system and a larger freedom in the control of deposition profile via an off-axis positioning of the front mirrors.

That plasma performance is significantly enhanced in the post-pellet periods cannot be explained solely by the increase in the plasma density. For comparison, a gas fuelled discharge *W7X20180920.017* with the heating power and line averaged density similar to the discussed pellet experiment is shown on the right hand side of figure 2. In this case the flat-top density is maintained by a feedback control of edge fuelling from a gas-puff system in addition to recycling from the first wall. The central electron temperature is similar to that in the enhanced phase of the pellet experiment, while the ion temperature is well below, in spite of having a sufficient electron-ion collisional coupling, as further discussed later in the paper. Furthermore, the diamagnetic plasma energy is considerably lower in the gas-fuelled example.

The increase in the plasma energy during the enhanced phase implies also an improvement in the global energy confinement time. A comparison of the experimental confinement time with the ISS04 scaling is given in figure 3 for the two discharges introduced above. The experimental values are estimated with and without the time derivative of the diamagnetic energy to demonstrate the contribution of the latter during

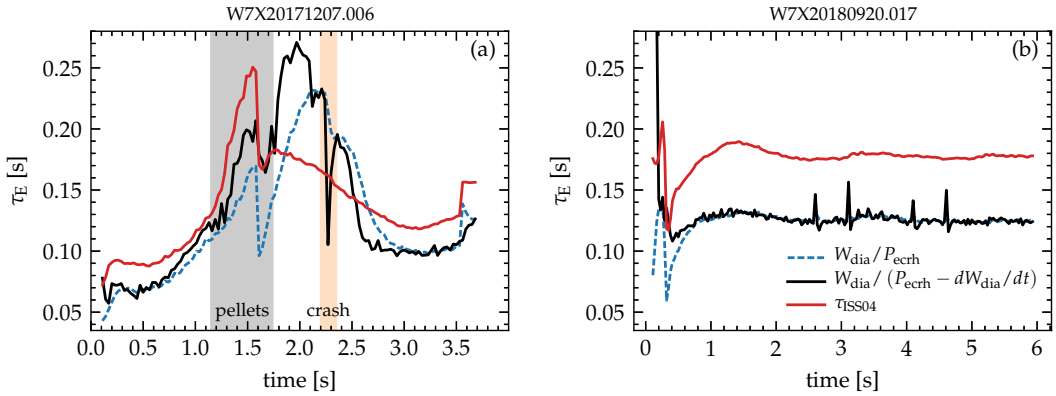

Figure 3: Comparison of the experimental global energy confinement time with the ISS04-scaling [2] for the two shots illustrated in figure 2. (a) - the pellet discharge with the enhanced phase; (b) - the gas-fuelled discharge. Short spikes between 2 and 5 s in the gas-fuelled discharge are caused by diagnostic NBI blips. For completeness, the experimental confinement time is calculated both with and without the time derivative of the diamagnetic energy. Both definitions coincide under stationary conditions. The color legend is the same for the two plots and is given in the right plot.

the post-pellet phase, with both definitions coinciding under stationary conditions. The ISS04 scaling is evaluated for the instantaneous plasma parameters. In the gas-fuelled discharge *W7X20180920.017*, figure 3b, the confinement time is at the level of 70% of the scaling during the flat-top part of the experiment, which is typical for gas-fuelled discharges at relevant parameters [66]. In contrast, the experimental confinement time often exceeds the scaling after pellet series, figure 3a. For instance, the experimental values are approximately 30% above the scaling during the short plateau phase of the diamagnetic energy in the discharge *W7X20171207.006*. This enhancement lasts for at least two confinement times and is partially weakened by an MHD event. The improvement in the global energy confinement time indicates a temporary change in the heat transport, which will be discussed in more detail in section 4.

The performance improvement after injections of pellet series as compared to gas-fuelled experiments at similar parameters is confirmed by an analysis of a large experimental database covering almost 90 minutes of cumulative plasma operation with ECRH heating. Several global plasma parameters realized in selected pellet experiments are compared to those from gas fuelled discharges in figure 4. Here, quantities of interest, including the plasma energy, β-values, ion temperature, energy confinement time and triple product, are plotted in color versus the line averaged electron density and heating power. For the gas fuelled cases, each point in the graph represents a quasi-stationary plasma state, i.e. with a small change in the main parameters, averaged over a time window of 200 ms. The operational space is defined by the available heating power and by the power dependant radiative density limit [31, 67]. Inside these boundaries, the operational space is densely covered and smooth dependencies of the global parameters

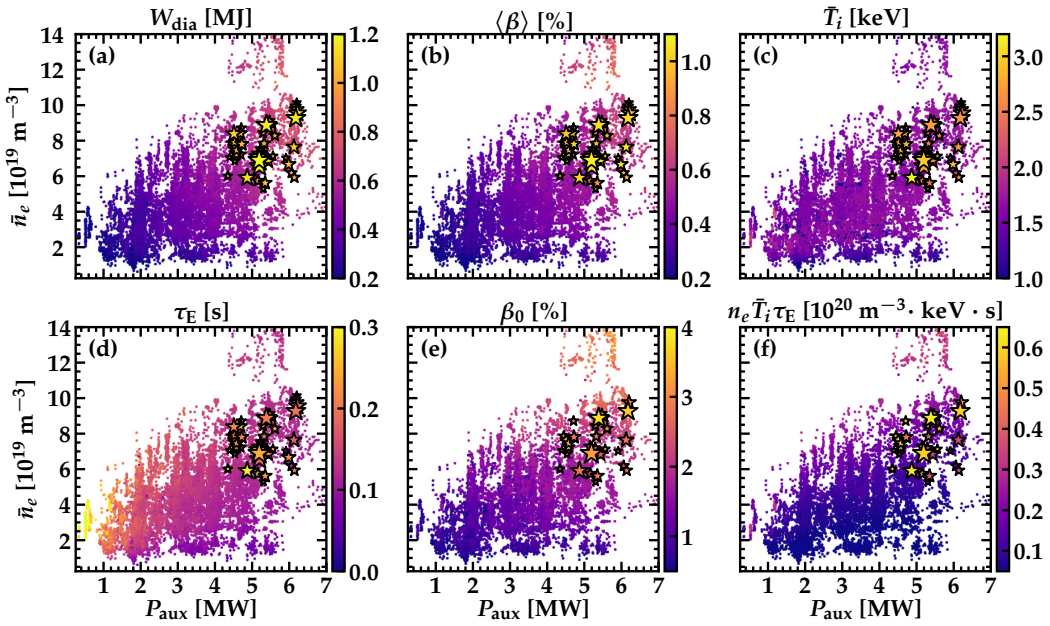

Figure 4: Overview of global plasma parameters in the gas-fuelled (dots) and high-performance pellet discharges (stars). Parameters of interest are encoded as colour. The colour scales, common to both sets of data, are shown next to each subplot. In addition, the stars are scaled in size according to the values they represent to highlight the highest achieved values. It can be seen that the values achieved in the pellet experiments are well above those in the gas-fuelled cases. (a) - the diamagnetic plasma energy measured with the diamagnetic loop; (b) - the volume averaged plasma β; (c) - the ion temperature averaged along a central line of sight of the XICS diagnostic; (d) - the global energy confinement time; (e) - the central plasma β_0 calculated from kinetic profiles, assuming $Z_{eff} = 1$; (f) - an estimation of the triple product.

on the density and power are evident. For example, the energy confinement time is found to deteriorate with the heating power and to improve with the density. Remarkably, almost no dependence on either density or power can be distinguished for the ion temperature above a low density threshold: the ion temperature remains below about 1.6 keV. The values from the pellet experiments, shown in stars, transiently but significantly surpass those from the gas-fuelled discharges at similar densities and heating powers. This can be perceived by comparing colours of the stars to background colours. The plasma stored energy, and consequently the energy confinement time, in the pellet cases is improved by more than 40%. Also, the ion temperature is raised to values above 3 keV with a typical ECRH power of 5 MW, the highest values obtained in W7-X so far and almost a factor of two higher than in typical gas-fuelled plasmas.

The post-pellet enhanced confinement phases are transient, usually lasting only several confinement times and decaying with the reduction of the density and of the density peaking. The exact conditions for the loss of high-performance are not well

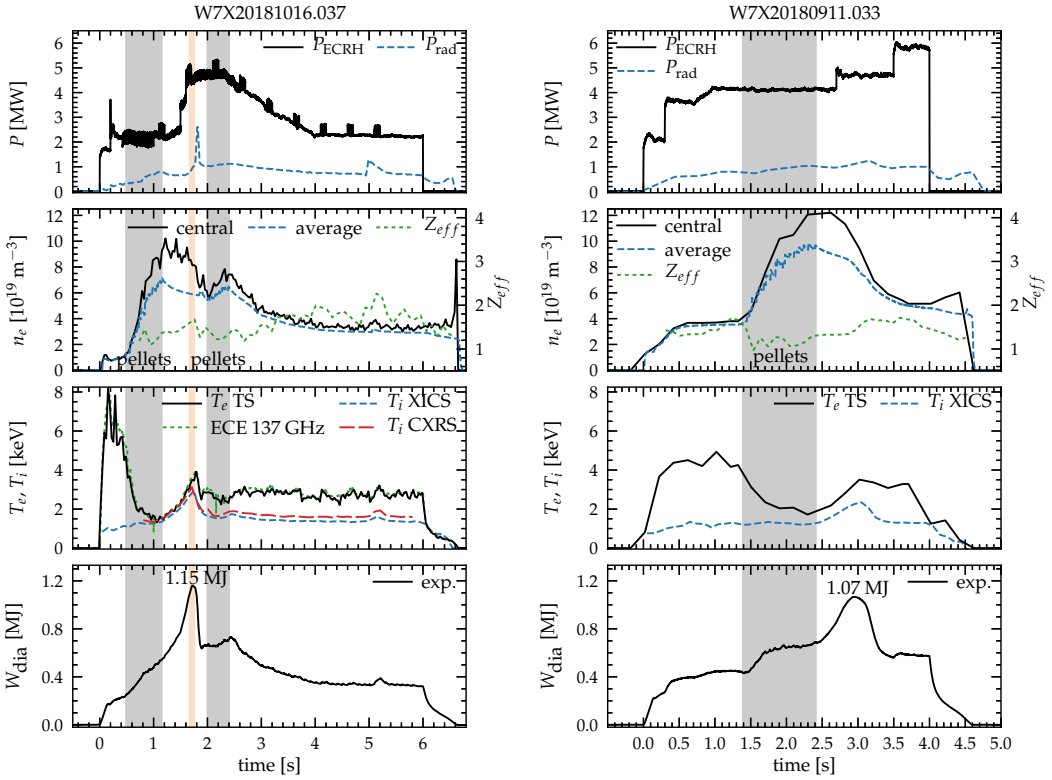

Figure 5: Two pellet discharges with enhanced phase. Left - standard magnetic configuration, ECRH in the X2-mode. In this case the high resolution CXRS diagnostic was available. The highest ion temperature point with available CXRS data is highlighted in orange. The gradual decrease of the heating power after 2.2 s was pre-programmed. Right - high-iota configuration, ECRH in the O2-mode. The breakdown and the initial part are realized with the X2-mode. A switch to the pure O2-heating was performed during the shot similar to [32].

understood yet. In some discharges MHD events appear to contribute to the confinement degradation. For example, a short event is present at about 2.25 s in the pellet shot in figure 2, as further discussed in section 3.3. A more detailed study of the improvement termination will be given in future publications.

About 15 pellet discharges, where the stored plasma energy was at or exceeded 1 MJ and the ion temperature was above usual values, were realized up to now, showing that the enhanced phases can be reliably reproduced. However, it is not possible to simply repeat a given control-waveform exactly, because of small variations in the initial density level, first wall conditions, pellet quality, etc. For example, another pellet discharge, *W7X20181016.037*, in the standard magnetic configuration is shown on the left of figure 5. In this case, the diamagnetic energy exceeds 1.1 MJ and the ion temperature reaches about 3 keV after the first pellet series. But, the enhanced phase is shorter as compared to the discharge *W7X20171207.006*. A second series of pellets was injected roughly 1 s after the first one. However, the improved phase after the second pellet

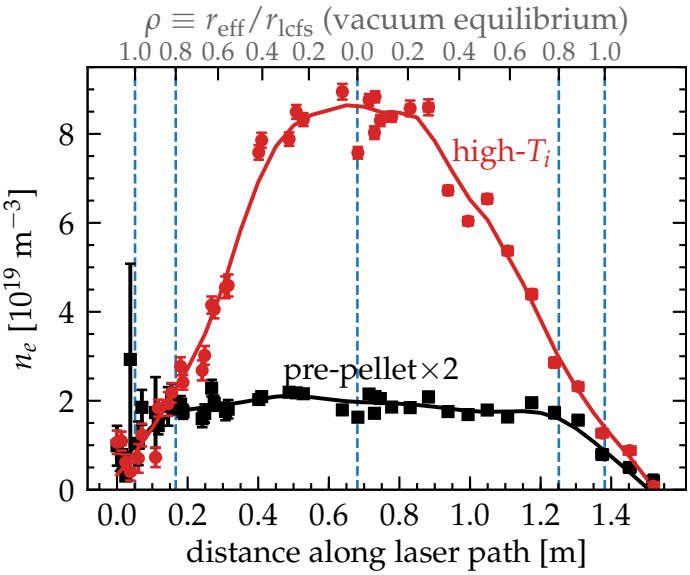

Figure 6: Density profiles before the pellet injection (0.35–0.42 s, black) and at the peak of ion temperature during the enhanced post-pellet phase (1.65–1.75 s, red) for the discharge *W7X20181016.037*. The profiles are plotted along the laser path of the Thomson diagnostic, that passes approximately horizontally through the plasma center close to the triangular cross-section. In addition, an approximate mapping to normalized radius is given on the top, using a vacuum equilibrium. Vertical dashed blue lines mark the separatrix, the $r/a = 0.8$ flux surface and the magnetic axis. The pre-pellet profile is scaled with a factor of two for the sake of clarity. The vertical error bars represent the statistical uncertainty of $\pm 1 \cdot \sigma$. The systematic errors, mainly due to drifts of the laser position, are typically dominant for the density profiles.

injection is not as pronounced, probably because of the weaker density peaking. The ion temperature in this discharge was also diagnosed with the high-resolution CXRS system using 10 ms short NBI blips with repetition rate of 10 Hz, in addition to the routine ion temperature measurements with XICS. Because of the availability of high resolution ion temperature profiles, this discharge is used for a power balance analysis later in the paper.

The enhanced post-pellet phases were successfully obtained in the standard and high-iota magnetic configurations. No clear difference in the plasma performance between the two configurations can be concluded yet, primarily due to poor statistics and variations in the initial conditions. Other magnetic configurations were not addressed systematically. An example of a pellet discharge in the high-iota magnetic configuration is shown on the right of figure 5. In this case, the ECRH system was switched to the O2-polarization during the initial phases before the pellet injection, as previously reported in [32]. The use of the O2-heating allowed to achieve a higher plasma density. However, a higher value of the heating power and a higher initial density were used to assure an acceptable level of the stray radiation during the O2-period. As a result, the final

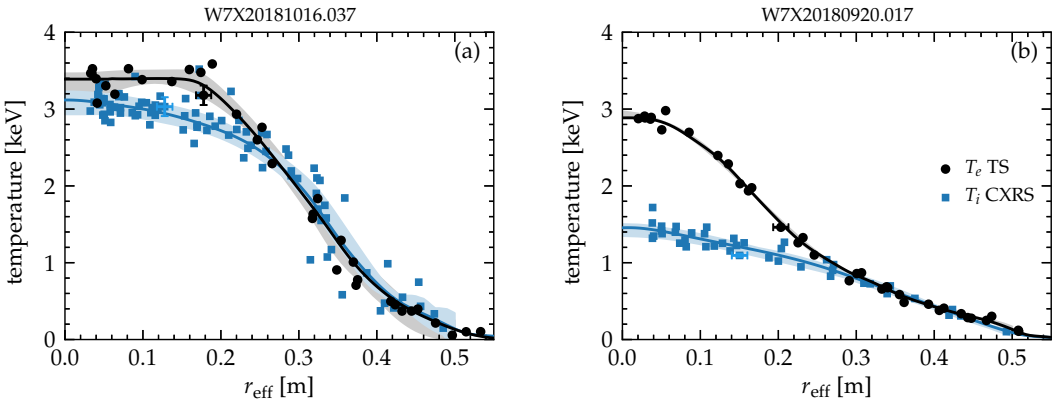

Figure 7: Electron (black) and ion (blue) temperature profiles. (a) - post-pellet phase with an enhanced confinement (1.67–1.75 s); (b) - gas-fuelled discharge at a comparable line averaged density (2.5–5.2 s). The electron temperature profiles are from the Thomson scattering system. The ion temperature profiles are from the CXRS system. The mapping of the measurement points to flux surfaces is performed with VMEC equilibria based on experimental pressure profiles. The statistical uncertainty of $\pm 1 \cdot \sigma$ is shown for selected points. These errors are negligible for the plot (b) because of a sufficiently long flat-top. Hence, the remaining scatter in the profiles is due to systematic errors. The colour bands show fit variations used in a sensitivity study of the power balance.

density peaking in the O2-discharges was at the same level as in the X2-experiments. The overall plasma performance during the post-pellet phase is also similar to that in the X2-discharges.

Since improved post-pellet phases are relatively short, no clear conclusions concerning impurity accumulation can be presently made. The line averaged value of Z_{eff} as measured with visible spectroscopy [68] can show an increase, as it is the case for discharge *20181016.037* in figure 5, but the final value is comparable with that in normal ECRH discharges. Therefore, further dedicated measurements of impurity confinement with a laser blow-off diagnostic or with a test impurity pellet injection appear necessary.

3.1. Density and temperature profiles

One prominent common feature of the pellet fuelled discharges is the occurrence of peaked density profiles. The full density profiles before and after the pellet injection are compared in figure 6. The density profiles are typically flat inside the normalized radius of about 0.8 for the gas-fuelled conditions. A significant density gradient usually exists only outside of this radius, as demonstrated with the pre-pellet situation in the figure, and the profile shape shows very little variation with the absolute value of the density. In contrast, with the injection of a series of hydrogen pellets, material is deposited relatively deep into the plasma core and the gradient region is extended as deep as to

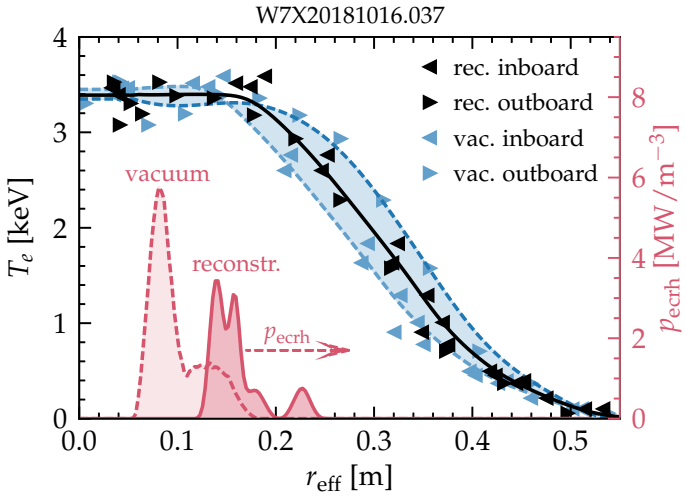

Figure 8: Equilibrium effects in the electron temperature profile. The inboard and outboard sides of the full profile Thomson scattering diagnostic are plotted with left and right triangles. Two branches of the profile mapped using an appropriate vacuum equilibrium are shown in dashed blue lines. The shaded blue region highlights the difference between the two sides. The temperature profile mapped using a VMEC calculation with an experimental pressure profile is shown in black. In addition, the ECRH deposition calculated with TRAVIS for the two equilibria is presented in red. The magnetic field is 2.52 T at the axis in the $\varphi = 0°$ plane for the vacuum equilibrium and is reduced for the finite-pressure one.

the normalized radius of 0.2–0.3. After the pellet injection, the density profiles gradually relax to the pre-pellet shape.

A typical pellet experiment is started at a rather low density, and, as a consequence, these plasmas are characterized by high electron temperatures strongly exceeding ion temperatures. During the pellet injection the electron temperature is strongly reduced, while the ion temperature is either moderately increased or not changed. After the end of the pellet series both temperatures grow and stay closely equilibrated during the enhanced confinement phase, reaching up to 3 keV at about 5 MW of electron heating. The ion temperature increase to such values cannot be explained by the collisional coupling alone, since the ion temperature remains at a much lower level in gas-fuelled experiments with similar parameters and, hence, a similar electron-ion power exchange. This observation is confirmed with the help of power balance analysis in section 4. To illustrate the difference between post-pellet and gas-fuelled plasmas, the electron and ion temperature profiles at the peak of the post-pellet phase in the shot *W7X20181016.037* are compared to those from a flat-top of the gas-fuelled discharge *W7X20180920.017* in figure 7. In the post-pellet case, there is a strong gradient in the ion temperature in the radial range between 0.2 and 0.4 m, whereas the ion temperature gradient is much shallower for the gas-fuelled example. At the same time, the central electron

temperatures are sufficiently close in the two cases. The difference in the electron temperature profile shape in the center, i.e. a peaked or a flat profile, can be explained by the location of the ECRH deposition. The flattening of the profile inside effective radius of about 0.2 m in the pellet case is caused by an off-axis ECRH deposition, as further detailed in the next section.

3.2. Equilibrium effects

The improved confinement in the post-pellet phases results in a non-negligible plasma pressure. The peak pressure values approach 1 atm corresponding to the peak β_0 of about 3.5%, estimated from kinetic profiles, and volume averaged $\langle\beta\rangle$ above 1%, measured with the diamagnetic loop, at the field of 2.5 T. The corresponding outward Shafranov shift of flux surfaces is observed with the full profile Thomson scattering system, figure 8. If a vacuum flux surface geometry is used to map the measurements, the inboard and outboard sides of the full profile do not agree and a gap of about 5–7 cm is observed between the two sides. The two profile sides can be brought to agreement by using an appropriate MHD equilibrium. VMEC calculations based on the experimental kinetic profiles indeed confirm that the magnetic axis is shifted by about 4 cm in the bean shaped plane and by about 6 cm in the triangular shaped plane relative to the vacuum position. The observed Shafranov shift appears consistent with the W7-X optimization, yet further studies are required to verify its scaling with the plasma pressure, rotational transform and magnetic configuration.

Finite plasma pressure also leads to a significant shift of the ECRH deposition into the high-field side direction, as previously found in a numerical study [69]. The shift is caused by a combination of the Shafranov shift and of a reduction of the absolute value of the magnetic field by diamagnetic currents, with both terms acting in the same direction. The field strength is reduced by roughly 0.1 T at the axis in the discharges of interest, which is sufficient for a noticeable change of the resonance position because of a relatively shallow field gradient.

An experimental confirmation of the finite-β effect on the ECRH deposition is shown in figure 8 and in more details in figure 9. A clear sign of the effect is the appearance of the off-axis heating resulting in a flattening of the electron temperature. The shape of the temperature profiles is consistent with the ECRH power density calculated with the help of the ray-tracing code TRAVIS [70], using suitable VMEC equilibria. A similar flattening of the electron temperature is otherwise found with an intentional off-axis ECRH operation via beam steering at low-β [71].

Figures 9(a-b) show a comparison of the normalized electron temperature from Thomson scattering with the predicted ECRH deposition at two representative times. Before the pellet injection the temperature profile is centrally peaked in agreement with the on-axis heating. During the high-β phase the temperature profile is flat inside the normalized radius of about 0.3. The edge of the flat part of the profile coincides with the location of the power deposition between $\rho = 0.25$ and $\rho = 0.32$. A correlation of the temperature

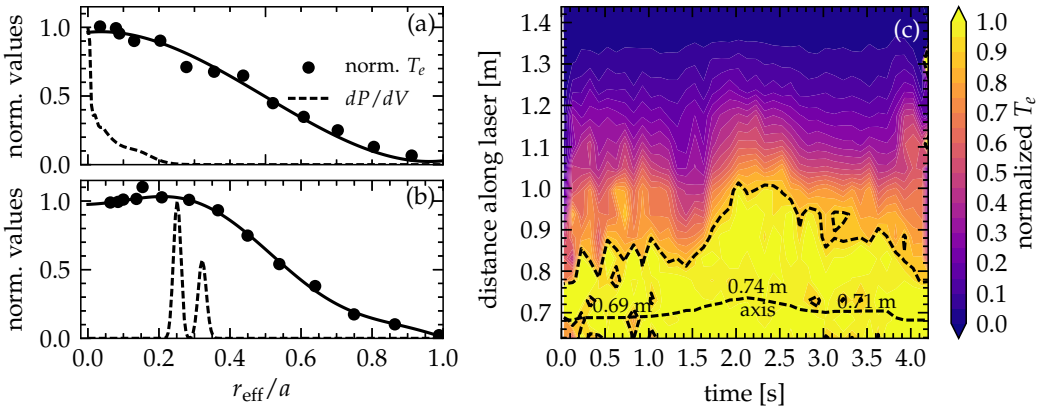

Figure 9: Shift of the ECRH deposition due to finite-β effects in the discharge *W7X20171207.006*. (a) - the normalized electron temperature (solid) and ECRH deposition from TRAVIS (dashed) before the pellet injection. (b) - the same for the high-β phase. (c) - a time evolution of the normalized temperature profile from Thomson scattering. The temperature data are given along the laser path. The 90% contour chosen to illustrate the profile width is stressed with thick dashed lines. The projection of the axis position is also indicated. Note, that for this discharge only the half profile Thomson scattering was available. The zero position of the distance was chosen to match the definition of figure 6.

flattening with the high-β phase is further demonstrated with the time evolution of the profile shape in local Thomson coordinates in figure 9c. Indeed, the profile broadening is present mainly during the enhanced post-pellet phase. For reference, the calculated magnetic axis position is also projected to the Thomson coordinates and indicates a Shafranov shift of about 5 cm. In this discharge, the settings for seven used ECRH beams were chosen in such a way as to heat at the normalized radius of about 0.05 without the finite-β effect.

The finite-β shift of the ECRH deposition can be compensated by starting the discharge at a higher value of magnetic field, in which case the temperature profiles are broadened during the low-β part of the discharge and become more peaked during the high-β part. For the achieved β-values, a vacuum field of 2.62 T is appropriate for the correction. Such a discharge was performed during the last campaign and the electron temperature profile was indeed found to be peaked [72]. However, it was also found that with such settings the electron and ion temperatures separate faster and the maximum ion temperature is below 2.5 keV. For this reason, a strong on-axis heating was not further pursued in these pellet experiments.

To summarize, a good agreement is found between the equilibrium calculations with VMEC and experiments. The comparison includes the mapping of different diagnostics to the flux surfaces, the prediction of the absolute value of the magnetic field and the estimation of the total plasma energy. These results emphasize reliability of the

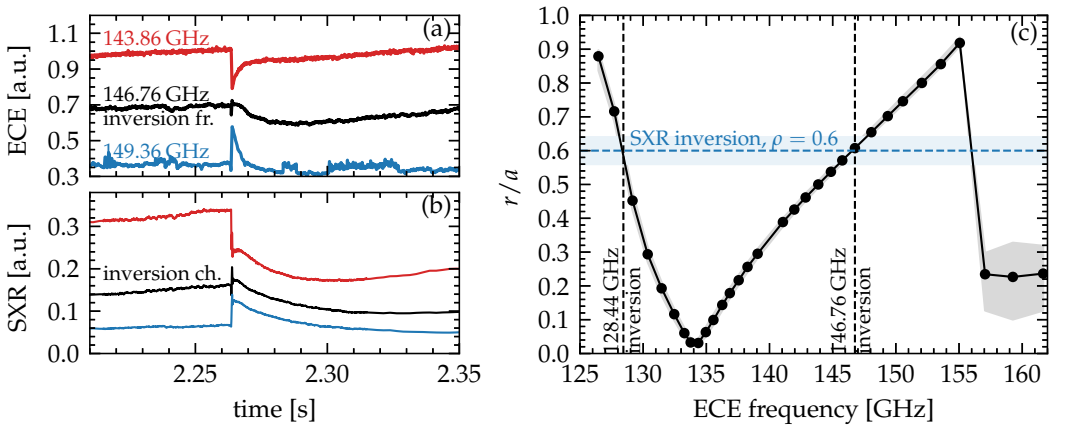

Figure 10: Details of the MHD event in the discharge *W7X20171207.006*. (a) - three selected ECE channels. (b) - three selected soft X-ray channels (20 soft X-ray cameras with 20 view lines each are available in total). (c) - the inversion radius observed with the soft X-ray cameras and with the ECE diagnostic. In the case of ECE, the inversion is observed both at the low field and high field sides.

numerical techniques and justify the use of such equilibria for further analysis.

3.3. Plasma stability

A sudden crash of the diamagnetic energy by about 150 kJ is observed at about 2.25 s, i.e. in the middle of the high energy phase, in the pellet discharge shown in figure 2. This event is detected with a number of other diagnostics and exhibits features of a fast MHD phenomenon taking place on a time scale much shorter than the typical confinement time. An inversion radius, similar to that in sawtooth events in tokamaks, is present in ECE and soft X-ray [73, 74] signals, as presented in figures 10(a-b). The core channels of these diagnostics demonstrate a quick drop on a timescale about 0.5 ms, whereas the edge channels show a quick rise of the signal. At the inversion radius (for ECE around channel 146.76 GHz at the high field side and channel 128.44 GHz at the low field side), no strong signal change is observed. Lines of sight showing the inversion could be identified for a subset of 17 (out of 20) available soft X-ray cameras and all of them are tangent to the same flux surface within 2 cm. The inversion frequency of the ECE was converted to the radial position using TRAVIS simulations and coincides with the inversion position of the soft X-ray diagnostic, see figure 10c.
The reason for this crash has not been clarified yet. The pressure profiles can be expected to be stable owing to the stability optimization of W7-X for β-values up to 5%. An alternative explanation might be a modification of the radial profile of the rotational transform (ι-profile) due to either bootstrap or ECRH driven currents. Although, the latter is expected to be low for the used gyrotron settings and the achieved electron density. Reconnection events are likely to occur, if the ι-profile crosses a low rational value, e.g. 5/6, 5/5, etc. This is the same mechanism as suspected to be responsible for

smaller scale, regular crashes obtained in W7-X with a strong intentional current drive with the ECRH system [75]. Further investigations of this event are ongoing and will be reported separately.

A large scale MHD activity has only been observed in the pellet program *W7X20171207.006*. Since it is difficult to reproduce a given pellet discharge exactly in this type of experiment, experimental conditions for the crash as well its importance for limiting the achievable plasma parameters are presently not clarified. The two further pellet examples given in figure 5 show no crashes, although coherent modes in the range between 30 and 60 kHz are detected at the peak of the diamagnetic energy with the help of a phase contrast imaging system [76]. The temperature and energy decay in the discharge *W7X20181016.037* takes place on a much slower time scale of tens of milliseconds and shows no signs of inversion.

4. Transport analysis

In this section, local power balance is applied with the aim of understanding the improvement in performance observed during the post-pellet phases. Volume integrals of power sinks and sources inside a flux surface are compared with the neoclassical energy fluxes through this surface both for electrons and ions. All values compared in the analysis are expressed in units of power. This formulation is similar to the one used for studies of the preceding experiment W7-AS [20, 77]. The neoclassical energy flux Q_α^{neo} includes both the diffusive q_α^{neo} and the convective $\Gamma_\alpha^{\mathrm{neo}} T$ terms. The power source and sink terms considered here are the ECRH heating power P_{ecrh}, the electron-ion power exchange term P_{ei}, the volume integral of the electric field term $e\Gamma_\alpha E_r$ and the radiative power loss P_{rad}.

Two representative discharges are chosen for the analysis. The first case is the highest ion temperature point observed with the CXRS system during the enhanced post-pellet phase in the discharge *W7X20181016.037*. This point is highlighted with a light orange color in figure 5. The second case is the flat-top state between 2.5 and 5.2 s of the gas-fuelled discharge *W7X20180920.017* at a similar line integrated density and heating power, illustrated on the right of figure 2.

In both discharges the ion temperature profiles were measured with the CXRS system, which is important to reliably estimate the collisional electron-ion power transfer, especially under conditions of a close temperature equilibration. In fact, the availability of the CXRS data is the main motivation to use the pellet discharge *W7X20181016.037*, where the system was operated in the high resolution mode, in spite of the improved phase being relatively short. The temperature profiles used for both discharges are given in figure 7. The density profiles are illustrated in figure 6.

The main components for the power balance are computed in the following way. All kinetic profiles, including temperatures, density and assumed flat Z_{eff}, are mapped to the flux surfaces using dedicated VMEC [63] equilibria as described in section 3.2. The ECRH power deposition is calculated with the ray-tracing code TRAVIS [70], see also

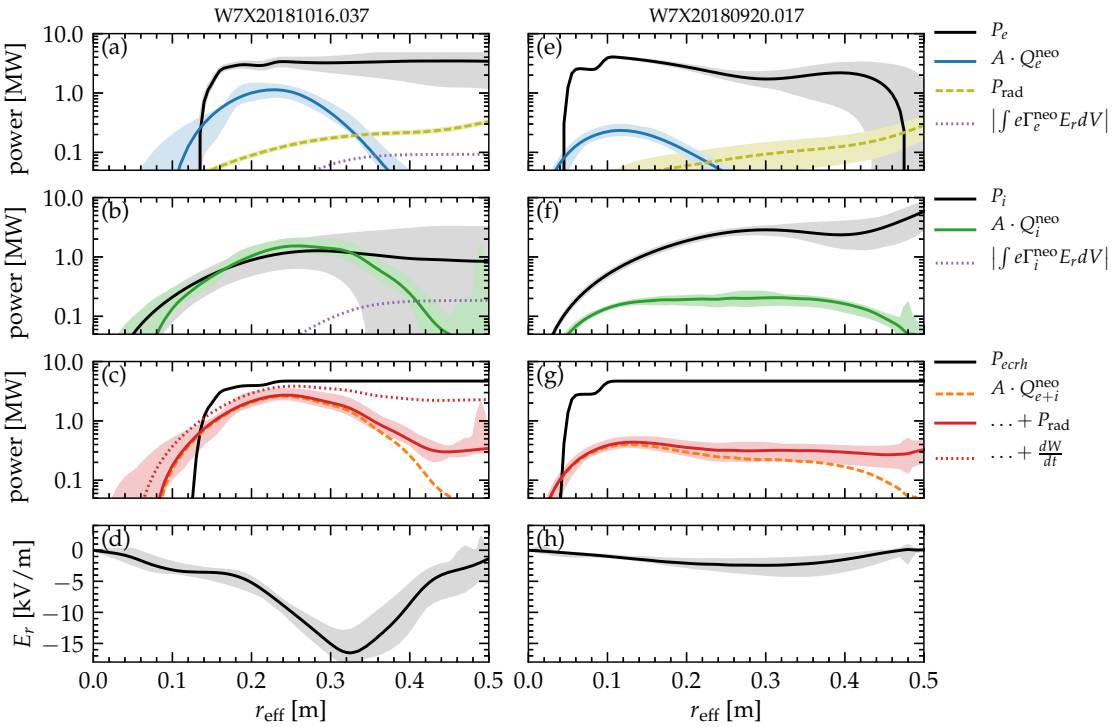

Figure 11: Power balance analysis (logarithmic scale). Left - an enhanced confinement phase after pellets. Right - a flat-top phase of a gas-fuelled discharge at similar parameters. (a), (e) - electron channel. Here, $P_e = P_{\rm ecrh} - P_{ei} - \int_0^r e\Gamma_e^{\rm neo} E_r dV - P_{\rm rad} \approx P_{\rm ecrh} - P_{ei}$, $A \equiv dV/dr$ (b), (f) - ion channel. Here, $P_i = P_{ei} + \int_0^r e\Gamma_i^{\rm neo} E_r dV \approx P_{ei}$ (c), (g) - combined balance. $Q_{e+i}^{\rm neo} \equiv Q_e^{\rm neo} + Q_i^{\rm neo}$. The total losses (solid red line) are $Q_{e+i}^{\rm neo} + P_{\rm rad}$. The total losses with the time derivative (dotted red line) are $Q_{e+i}^{\rm neo} + P_{\rm rad} + \frac{dW}{dt}$, where $W(r)$ is the kinetic plasma energy inside a flux surface. (d), (h) - ambipolar radial electric field E_r.

figures 8 and 9. Mono-energetic neoclassical transport coefficients are calculated with the drift kinetic equation solver DKES [78, 79]. The radial electric field E_r, which is important for the neoclassical transport, as discussed e.g. in [26], is derived from the ambipolarity condition on the neoclassical particle fluxes. The computed E_r can be found in figures 11d,h. This approximation was recently validated in W7-X experiments with the help of the XICS diagnostic [56, 80] and will be further investigated with the CXRS system. For the power term $e\Gamma_\alpha E_r$, the particle flux is assumed to be neoclassical. In any case, experimental particle fluxes in the core are sufficiently small for this term not to play a major role. The radiated power is estimated from a tomographic inversion of data from the bolometry system [60]. Finally, the power balance analysis is performed by means of the 1d transport code NTSS [81, 82].

Results of the power balance analysis are summarized in figure 11 for the electron and ion channels separately, as well as for the combined power. During the post-pellet enhanced confinement phase, shown in the three panels on the left of the figure, the neoclassical

ion heat flux corresponds closely to the ion input power inside two thirds of the plasma radius. Here, the input power is primarily the collisional electron-ion exchange. In the outer one third of the plasma radius, where the ion temperature decays quickly, see figure 7a, the neoclassical heat flux alone is not sufficient to explain the losses, at least for profile fits maintaining equal electron and ion temperatures in this outer part. The neoclassical heat flux for electrons covers between 20% and 40% of the electron input power inside 30 cm ($r_{\mathrm{eff}}/a < 0.6$). In the outer region, a significant fraction of the input power is not explained by the neoclassical theory also for electrons. The radiated power is generally low in the plasma core and becomes important only at the edge. The combined neoclassical losses are at the level of about 50% of the input ECRH power up to about 30 cm. At the edge, where the plasma is cold and potentially also charge-exchange losses can contribute, up to a factor of 10 is missing. It can be concluded that the neoclassical transport is a significant component of the total transport in the plasma core during the enhanced periods.

The power balance analysis for the post-pellet period described above is not perfectly complete, because the plasma during this interval is not truly stationary. Even if the total plasma energy is constant, the kinetic profiles are not static. Furthermore, the analysis time point, chosen based on the availability of the CXRS data, is at the edge of the flat portion of the diamagnetic energy curve, see figure 5. If an estimation of the time derivative of the kinetic energy inside a flux surface is added to the loss terms, up to 80% of the input power is explained in the core and up to 50% at the edge, as illustrated with a dotted line in figure 11c. These values are likely to represent an upper boundary of the power balance, since at the maximum the time derivatives can be expected to become negligible. For a more confident estimation of the derivatives the time resolution of the profile diagnostics needs to be improved.

In order to quantify uncertainties in the power balance, a variation of profile fits for the density and for both temperatures was performed in a manner similar to e.g. [83]. This includes a change of the fit inside experimental error bars, a change of the fit functional form, a change of the equilibrium used and a legitimate shift of profiles by up to 1 cm. This value for the profile shift is due to experimental uncertainties in the measurement locations and due to a finite size of the measurement volumes. In addition, the Z_{eff} value was varied between one and two, where the measured value is about 1.5 [68]. The resulting uncertainties for selected quantities are illustrated in figure 11 with coloured bands. For example, the uncertainties cover the edge of the ECRH deposition between 10 and 14 cm. Consequently, the electron power balance in this range is susceptible to the nuances of profile fits. Besides, the electron-ion exchange power can be observed, see figure 11b outside of 0.3 m, to be sensitive to the relative position of the two temperature profiles, which is to be expected for the closely equilibrated conditions. Nevertheless, these uncertainties do not change the main finding, that the neoclassical transport is significant during the enhanced confinement periods. It is in fact during such phases that one could attempt to verify the importance of the neoclassical optimization.

The combined power balance shows similar results also for other pellet discharges with

an enhanced phase. For example, it is found also for the discharge *W7X20171207.006* that the total neoclassical heat flux is in the range of 40% to 50% of the input power in the core [72, 80]. But a separation of the electron and ion channels in other discharges is complicated due to the absence of CXRS profiles, as previously noted.

The picture is different for the gas-fuelled discharges, despite a similar level of the ECRH heating power and a similar value of the line averaged density. A gap of about a factor of ten is present both for electrons and ions and, hence, for the combined balance. In the latter case, the missing fraction is roughly uniform throughout the plasma. This means that a strong anomalous loss mechanism dominates and determines the heat flux across the entire plasma cross section, whereas the neoclassical transport is a minor contribution. The much lower ion temperature in the discharge *W7X20180920.017* compared to the post-pellet case, in spite of two times higher ion input power, cannot be explained without such an additional loss mechanism. We note that the decrease in the electron input power between 0.1 and 0.3 m and the successive minor rise (figure 11d) are mainly due to the power transfer to the ions. The rising part after 0.3 m is likely an analysis artefact that originates from a slight misalignment of closely equilibrated electron and ion temperature profiles.

A plausible candidate to explain the anomalous losses is the ion-scale turbulence, caused by the ion-temperature gradient instability (ITG), which is typically unstable in simulations under normal W7-X operational conditions (ECRH heating and gas fuelling, similar to the conditions without pellets). The ITG mode experiences a strong reduction in the presence of a density gradient, for example after pellet injections, similar to tokamaks [84, 85]. However, in W7-X this reduction is particularly favourable, since the trapped electron modes (TEM), associated to the density gradient, are decreased due to the maximum-J property [21]. Therefore, a window with reduced growth rate exists in the parameter space of electrostatic instabilities (stability map) as found with linear GENE simulations [22,86]. Experimentally, it is indeed observed that the relative magnitude of ion-scale ($k_\perp \rho_s \approx 1$) broad band density fluctuations as measured with a phase contrast imaging system [76] is reduced during such enhanced phases, and their distribution in the wavenumber space is significantly modified [87]. Another relevant element for the turbulence reduction is the ion-root radial electric field, which becomes significant after pellet injections, following the peak of the density gradient [80]. The electric field is thought to be responsible for the turbulence stabilization also in non-axisymmetric configurations lacking the maximum-J property, like optimum confinement in W7-AS [17–19]. A theoretical analysis is currently ongoing, with the aim to address the corresponding impact of these mechanisms.

One of significantly improved parameters in the enhanced post-pellet phases is the ion temperature, see for example figures 2 and 7. Hence, this quantity may serve as an indicator of the improved transport. The achieved ion temperature is found to correlate with the core density peaking introduced by pellet injection. Figure 12a shows a scaling of the ion temperature at the peak with the density peaking at the same time for a set of pellet discharges. In general, high ion temperatures correspond to a pronounced

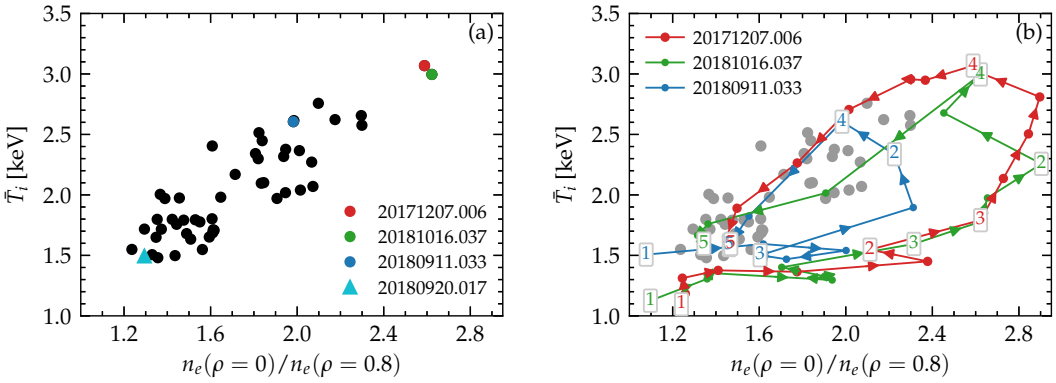

Figure 12: Correlation of the ion temperature with the density peaking. (a) - values at the peak of ion temperature for a set of pellet discharges (black). The discharges discussed in the paper are shown in different colors. The comparison gas-fuelled discharge *W7X20180920.017* is illustrated with a triangle. (b) - shot trajectories for three selected discharges illustrated previously in the paper. The marked time moments are: 1 - start of the pellet injection; 2 - power step; 3 - end of the pellet injection; 4 - peak of the ion temperature; and 5 - full relaxation of the post-pellet phases.

density peaking. Here, the density peaking is defined as the ratio of the density close to the axis to that at the normalized radius of 0.8. As previously discussed for figure 6, this ratio is representative of a density gradient in the range $\rho = 0.2$–0.8. The data for gas-fuelled discharges are located in the lower left corner of the dependence, i.e. they are characterized by flat density profiles and low ion temperatures, as illustrated with the comparison discharge *W7X20180920.017* in the figure.

The evolution of density peaking in selected pellet experiments is illustrated in figure 12b for three discharges discussed previously in the paper. The trajectories are plotted with a constant time step of 100 ms. Initially, all discharges start with rather flat density profiles (time moment 1). At the end of the pellet injection, a noticeable density peaking is introduced (time moment 3). The increase of the heating power (time moment 2) seems to slightly decrease the peaking. The peaking further increases after the pellet injection due to the low recycling conditions. The ion temperature grows at the same time and eventually reaches a maximum value. After the peak, the ion temperature decays together with the density peaking. The decay period is especially well tracked in the discharge *W7X20171207.006*, where the relaxation is rather gradual. These results suggest the importance of controlling the density profile shape for enhanced performance in W7-X. A further analysis of gradient lengths will be published later.

5. Summary

In recent W7-X experiments, injections of cryogenic hydrogen pellets were successfully applied for core plasma fuelling. Plasma periods with enhanced confinement properties were observed after the pellet injections. These periods are transient, a few confinement times only, but reproducible. Up to now, about 15 pellet discharges with a clearly enhanced performance in the post-pellet phase were realized.

The post-pellet periods are of interest due to their prominent plasma parameters. The ion temperature reaches central values above 3 keV with the ECRH heating of about 5 MW. The diamagnetic plasma energy is up to 1.2 MJ, corresponding to the volume averaged β above 1% and central β_0 above 3.5% at the field of 2.5 T. The global energy confinement time transiently exceeds the empirical stellarator scaling ISS04 by about 30%. The simultaneous improvement in the ion temperature and in the confinement time implies a high value of the triple product, as reported previously [3].

First signs of equilibrium effects are observed during the enhanced periods. The Shafranov shift in the triangular plane is measured to be up to 6 cm. Reducing Shafranov shift in high-β stellarator plasmas is essential for maintaining closed flux surfaces and, therefore, was one of the major W7-X design points. The first measurements appear consistent with the optimization, but, obviously, further studies are required for a conclusive validation. Finite plasma pressure also leads to a significant shift of the ECRH deposition due to a combination of the Shafranov shift and of a diamagnetic reduction of the magnetic field.

Plasma parameters achieved in the pellet experiments could not be reproduced in gas-fuelled ECRH discharges. With a similar input power and line averaged electron density of about $6 \cdot 10^{19}$ m^{-3}, the ion temperature is only about 1.6 keV and the confinement time is about 70% of the ISS04-scaling. Moreover, the ion temperature remains below 1.6 keV in the whole range of the available ECRH power and achievable densities.

Following the neoclassical optimization, W7-X was expected to outperform the ISS04-scaling in ECRH plasmas with a relatively flat density profile by a factor of two [81]. The local power balance analysis in section 4 shows that in gas-fueled plasmas this is hindered by anomalous losses, with the anomalous heat fluxes being about a factor of 10 larger than the neoclassical ones. The anomalous losses are strongly reduced and, as a consequence, the neoclassical fluxes become more important in the post-pellet phases. It can be expected that these are the conditions where the transport optimization of W7-X should be more apparent. To this end, future experiments will verify dependence of the post-pellet plasma parameters on the effective helical ripple.

A possible explanation for the anomalous loss channel in the gas-fuelled discharges is the ion-scale turbulence. In particular, ion temperature gradient modes are predicted to be unstable under normal W7-X conditions. It is also known, similar to tokamaks, that the ITG turbulence can be stabilized by a density gradient at the location of the ion temperature gradient. At the same time, trapped electron modes are more stable in the W7-X geometry due to the maximum-J property [21]. These two facts lead to

a formation of a stability region [22], which may explain the improved performance in the post-pellet phases. The correlation between the ion temperature and the density peaking in the pellet experiments is qualitatively consistent with this hypothesis. A more detailed analysis of the fluctuation diagnostics, of the gradient lengths and of the role of the radial electric field is to follow.

The results of this work suggest importance of controlling the shape of density profiles for the high performance operation in W7-X. Presently, peaked profiles can be achieved transiently with the pellet injection, while the gas fuelling usually results in flat profiles. To improve the profile control and to extend it to a steady state or at least to a periodic operation, the W7-X capabilities are being improved with the installation of a continuous pellet injector and of a cryopump system. The new pellet injector will be able to provide core particle fuelling, while the improved pumping will help to maintain the edge density at a low level. Neutral beam injection and wall preconditioning for low recycling are further possible tools to control the profile shape. In the preceding experiment W7-AS, NBI-heating was extensively used to realize improved confinement regimes such as an optimum confinement regime [17–19] similar to the post-pellet phases in many respects and a high density H-mode [19, 88] with improved energy confinement, reduced impurity confinement and high separatrix density. All new experimental options will be extensively explored in future W7-X campaigns to prolong the already achieved good confinement properties.

6. Acknowledgments

This work has been carried out within the framework of the EUROfusion Consortium and has received funding from the Euratom research and training programme 2014-2018 and 2019-2020 under grant agreement No 633053. The views and opinions expressed herein do not necessarily reflect those of the European Commission.

References

[1] Baldzuhn J, Damm H, Beidler C D, McCarthy K, Panadero N, Biedermann C, Bozhenkov S A, Brunner K J, Fuchert G, Kazakov Y, Beurskens M, Dibon M, Geiger J, Grulke O, Höfel U, Klinger T, Köchl F, Knauer J, Kocsis G, Kornejew P, Lang P T, Langenberg A, Laqua H, Pablant N A, Pasch E, Pedersen T S, Ploeckl B, Rahbarnia K, Schlisio G, Scott E R, Stange T, von Stechow A, Szepesi T, Turkin Y, Wagner F, Winters V, Wurden G and and D Z 2019 Plasma Physics and Controlled Fusion **61** 095012 https://doi.org/10.1088%2F1361-6587%2Fab3567

[2] Yamada H, Harris J, Dinklage A, Ascasibar E, Sano F, Okamura S, Talmadge J, Stroth U, Kus A, Murakami S, Yokoyama M, Beidler C, Tribaldos V, Watanabe K and Suzuki Y 2005 Nuclear Fusion **45** 1684–1693 https://doi.org/10.1088%2F0029-5515%2F45%2F12%2F024

[3] Pedersen T S, König R, Krychowiak M, Jakubowski M, Baldzuhn J, Bozhenkov S, Fuchert G, Langenberg A, Niemann H, Zhang D, Rahbarnia K, Bosch H S, Kazakov Y, Brezinsek S, Gao Y and and N P 2018 Plasma Physics and Controlled Fusion **61** 014035 https://doi.org/10.1088%2F1361-6587%2Faaec25

[4] Wolf R C, Bozhenkov S, Dinklage A, Fuchert G, Kazakov Y O, Laqua H P, Marsen S, Marushchenko N B, Stange T, Zanini M, Abramovic I, Alonso A, Baldzuhn J, Beurskens M, Beidler C D, Braune

H, Brunner K J, Chaudhary N, Damm H, Drewelow P, Gantenbein G, Gao Y, Geiger J, Hirsch M, Höfel U, Jakubowski M, Jelonnek J, Jensen T, Kasparek W, Knauer J, Korsholm S B, Langenberg A, Lechte C, Leipold F, Mora H T, Neuner U, Nielsen S K, Moseev D, Oosterbeek H, Pablant N, Pasch E, Plaum B, Pedersen T S, Sitjes A P, Rahbarnia K, Rasmussen J, Salewski M, Schilling J, Scott E, Stejner M, Thomsen H, Thumm M, Turkin Y and and F W 2018 Plasma Physics and Controlled Fusion **61** 014037 https://doi.org/10.1088%2F1361-6587%2Faaeab2

[5] Milora S, Houlberg W, Lengyel L and Mertens V 1995 Nuclear Fusion **35** 657–754 https://doi.org/10.1088%2F0029-5515%2F35%2F6%2Fi04

[6] Greenwald M, Gwinn D, Milora S, Parker J, Parker R, Wolfe S, Besen M, Camacho F, Fairfax S, Fiore C, Foord M, Gandy R, Gomez C, Granetz R, LaBombard B, Lipschultz B, Lloyd B, Marmar E, McCool S, Pappas D, Petrasso R, Pribyl P, Rice J, Schuresko D, Takase Y, Terry J and Watterson R 1984 Phys. Rev. Lett. **53**(4) 352–355 https://link.aps.org/doi/10.1103/PhysRevLett.53.352

[7] Tubbing B, Balet B, Bartlett D, Challis C, Corti S, Gill R, Gormezano C, Gowers C, von Hellermann M, Hugon M, Jacquinot J, Jaeckel H, Kupschus P, Lawson K, Morsi H, ORourke J, Pasini D, Rimini F, Sadler G, Schmidt G, Start D, Stubberfield P, Tanga A and Tibone F 1991 Nuclear Fusion **31** 839–850 https://doi.org/10.1088%2F0029-5515%2F31%2F5%2F003

[8] Smeulders P, Appel L, Balet B, Hender T, Lauro-Taroni L, Stork D, Wolle B, Ali-Arshad S, Alper B, Blank H D, Bures M, Esch B D, Giannella R, Konig R, Kupschus P, Lawson K, Marcus F, Mattioli M, Morsi H, OBrien D, ORourke J, Sadler G, Schmidt G, Stubberfield P and Zwingmann W 1995 Nuclear Fusion **35** 225–242 https://doi.org/10.1088%2F0029-5515%2F35%2F2%2Fi13

[9] Maget P, Garbet X, Géraud A and Joffrin E 1999 Nuclear Fusion **39** 949–962 https://doi.org/10.1088%2F0029-5515%2F39%2F7%2F311

[10] Baylor L R, Jernigan T C, Combs S K, Houlberg W A, Murakami M, Gohil P, Burrell K H, Greenfield C M, Groebner R J, Hsieh C L, La Haye R J, Parks P B, Staebler G M, Schmidt G L, Ernst D R, Synakowski E J and Porkolab M 2000 Physics of Plasmas **7** 1878–1885 (*Preprint* https://doi.org/10.1063/1.874011) https://doi.org/10.1063/1.874011

[11] Gruber O, Fahrbach H U, Gehre O, Herrmann W, Kaufmann M, Lackner K, Mertens V, Muller E R, Soldner F, Wagner F, Wunderlich R, Becker G, Bomba B, Bruhns H, Buchl K, Carlson A, Dodel G, Eberhagen A, Fussmann G, Gentle K, Giannone L, v Gierke G, Glock E, v Goeler S, Haas G, Hofmann J, Holzhauer E, Hubner K, Janeschitz G, Kaesdorf S, Karger F, Kluber O, Kornherr M, Krieger K, Lang R, Lee P, Lisitano G, Lorcher M, Luce T C, Mast F, Mayer H M, McCormick K, Meisel D, Miura Y, Murmann H, Neuhauser J, Niedermeyer H, Nolte R, Notredaeme J M, Petrov M P, Poschenrieder W, Rapp H, Rohr H, Roberts D E, Rudji A, Sandmann W, Schneider F, Schneider U, Siller G, Simmet E, Speth E, Stabler A, Steinmetz K, Steuer K H, Stroth U, Tsois N, Vollmer O, Whitley J B, Wurz H and Zasche D 1988 Plasma Physics and Controlled Fusion **30** 1611–1623 https://doi.org/10.1088%2F0741-3335%2F30%2F11%2F020

[12] Yamada H, Sakamoto R, Sakakibara S, Morita S, Tanaka K, Narihara K, Masuzaki S, Watanabe K, Peterson B, Osakabe M, Murakami S, Baylor L, Combs S, Goto M, Ida K, Idei H, Kaneko O, Kawahata K, Komori A, Kubo S, Miyazawa J, Nakanishi H, Narushima Y, Ohdahi S, Ohyabu N, Shoji M, Toi K, Tokuzawa T, Tsumori K and LHD Experimental Group 2000 Characteristics of pellet penetration and related performance improvement in LHD 27th EPS Conference on Contolled Fusion and Plasma Physics Budapest vol 24B (2000) pp 1320–1323 http://epsppd.epfl.ch/Buda/pdf/p4_015.pdf

[13] Sakamoto R, Yamada H, Tanaka K, Narihara K, Morita S, Sakakibara S, Masuzaki S, Inagaki S, Baylor L, Fisher P, Combs S, Gouge M, Kato S, Komori A, Kaneko O, Ashikawa N, de Vries P, Emoto M, Funaba H, Goto M, Ida K, Idei H, Ikeda K, Isobe M, Kado S, Kawahata K, Khlopenkov K, Kubo S, Kumazawa R, Minami T, Miyazawa J, Morisaki T, Murakami S, Muto S, Mutoh T, Nagayama Y, Nakamura Y, Nakanishi H, Nishimura K, Noda N, Notake

T, Kobuchi T, Liang Y, Ohdachi S, Ohyabu N, Oka Y, Osakabe M, Ozaki T, Pavlichenko R, Peterson B, Sagara A, Saito K, Sasao H, Sasao M, Sato K, Sato M, Seki T, Shimozuma T, Shoji M, Sudo S, Suzuki H, Takechi M, Takeiri Y, Tamura N, Toi K, Tokuzawa T, Torii Y, Tsumori K, Yamada I, Yamaguchi S, Yamamoto S, Yoshimura Y, Watanabe K, Watari T, Yamazaki K, Hamada Y, Motojima O and Fujiwara M 2001 Nuclear Fusion **41** 381–386 https://doi.org/10.1088%2F0029-5515%2F41%2F4%2F304

[14] Romanelli M, Bourdelle C and Dorland W 2004 Physics of Plasmas **11** 3845–3853 (*Preprint* https://doi.org/10.1063/1.1766031) https://doi.org/10.1063/1.1766031

[15] Horton W 2017 Turbulent Transport in Magnetized Plasmas 2nd ed (WORLD SCIENTIFIC) (*Preprint* https://www.worldscientific.com/doi/pdf/10.1142/10595) https://www.worldscientific.com/doi/abs/10.1142/10595

[16] Wagner F and Stroth U 1993 Plasma Physics and Controlled Fusion **35** 1321–1371 https://doi.org/10.1088%2F0741-3335%2F35%2F10%2F002

[17] Stroth U, Baldzuhn J, Geiger J, Geist T, Giannone L, Hirsch M, Jaenicke R, Kick M, Koponen J P, Kühner G, Penningsfeld F P, Wagner F and and 1998 Plasma Physics and Controlled Fusion **40** 1551–1565 https://doi.org/10.1088%2F0741-3335%2F40%2F8%2F008

[18] Kick M, Maaßberg H, Anton M, Baldzuhn J, Endler M, Grner C, Hirsch M, Weller A and and S Z 1999 Plasma Physics and Controlled Fusion **41** A549–A559 https://doi.org/10.1088%2F0741-3335%2F41%2F3a%2F048

[19] Hirsch M, Baldzuhn J, Beidler C, Brakel R, Burhenn R, Dinklage A, Ehmler H, Endler M, Erckmann V, Feng Y, Geiger J, Giannone L, Grieger G, Grigull P, Hartfu H J, Hartmann D, Jaenicke R, Knig R, Laqua H P, Maaberg H, McCormick K, Sardei F, Speth E, Stroth U, Wagner F, Weller A, Werner A, Wobig H, Zoletnik S and for the W7-AS Team 2008 Plasma Physics and Controlled Fusion **50** 053001 http://stacks.iop.org/0741-3335/50/i=5/a=053001

[20] Beidler C D, Feng Y, Geiger J, Kchl F, Maberg H, Marushchenko N B, Nhrenberg C, Smith H M and Turkin Y 2018 Plasma Physics and Controlled Fusion **60** 105008 http://stacks.iop.org/0741-3335/60/i=10/a=105008

[21] Proll J H E, Helander P, Connor J W and Plunk G G 2012 Phys. Rev. Lett. **108**(24) 245002 https://link.aps.org/doi/10.1103/PhysRevLett.108.245002

[22] Alcuson J 2018 Drift-wave instabilities in wendelstein 7-x plasmas 23rd Joint EU-US Transport Task Force Meeting (11 – 14 September 2018, Seville, Spain) http://www.psft.eu/ttf2018/wp-content/uploads/2018/06/alcuson-belloso_abstract_ttf2018.pdf

[23] Grieger G, Beidler C, Harmeyer E, Junker J, Kißlinger J, Lotz W, Merkel P, Montvai A, Nührenberg J, Rau F, Schlüter A, Wobig H and Zille R 1989 Physics studies for helical-axis advanced stellarators Plasma Physics and Controlled Nuclear Fusion Research, Proceedings of the 12th International Conference, Nice, 1988 vol 2 (IAEA, Vienna) pp 369 – 387

[24] Beidler C, Grieger G, Herrnegger F, Harmeyer E, Kißlinger J, Lotz W, Maaßberg H, Merkel P, Nührenberg J, Rau F, Sapper J, Sardei F, Scardovelli R, Schlüter A and Wobig H 1990 Fusion Technology **17** 148–168

[25] Wolf R C, Beidler C D, Dinklage A, Helander P, Laqua H P, Schauer F, Pedersen T S and Warmer F 2016 IEEE Transactions on Plasma Science **44** 1466–1471 ISSN 0093-3813

[26] Beidler C, Allmaier K, Isaev M, Kasilov S, Kernbichler W, Leitold G, Maaberg H, Mikkelsen D, Murakami S, Schmidt M, Spong D, Tribaldos V and Wakasa A 2011 Nuclear Fusion **51** 076001 http://stacks.iop.org/0029-5515/51/i=7/a=076001

[27] Helander P 2014 Reports on Progress in Physics **77** 087001 http://stacks.iop.org/0034-4885/77/i=8/a=087001

[28] Maaßberg H, Beidler C D and Simmet E E 1999 Plasma Physics and Controlled Fusion **41** 1135 http://stacks.iop.org/0741-3335/41/i=9/a=306

[29] Feng Y, Beidler C, Geiger J, Helander P, Hölbe H, Maassberg H, Turkin Y, Reiter D and W7-X Team 2016 Nuclear Fusion **56** 126011 http://stacks.iop.org/0029-5515/56/i=12/a=126011

[30] Klinger T, Andreeva T, Bozhenkov S A, Brandt C, Burhenn R, Buttenschön B, Fuchert G, Geiger

B, Grulke O, Laqua H P, Pablant N A, Rahbarnia K, Stange T, von Stechow A, Tamura N, Thomsen H, Wegner T and Bussiahn R 2019 Nuclear Fusion http://iopscience.iop.org/10.1088/1741-4326/ab03a7

[31] Fuchert G, Bozhenkov S, Burhenn R, Jakubowski M, Niemann H, Pasch E, Pedersen T S, Zhang D, Wolf R C, Wendelstein T and Wurden G A 2017 Density related operational limit in the limiter phase of Wendelstein 7-X 2017 European Conference on Circuit Theory and Design (ECCTD) pp 1–4 ISSN 2474-9672

[32] Laqua, HP, Baldzuhn, J, Braune, H, Bozhenkov, S, Brunner, KJ, Kazakov, YeO, Marsen, S, Moseev, D, Stange, T, Wolf, RC, Zanini, M and Wendelstein7-X Team 2019 EPJ Web Conf. **203** 02002 https://doi.org/10.1051/epjconf/201920302002

[33] Dibon M, Baldzuhn J, Beck M, Cardella A, Kchl F, Kocsis G, Lang P, Macian-Juan R, Ploeckl B, Szepesi T and Weisbart W 2015 Fusion Engineering and Design **98-99** 1759 – 1762 ISSN 0920-3796 proceedings of the 28th Symposium On Fusion Technology (SOFT-28) http://www.sciencedirect.com/science/article/pii/S0920379615000782

[34] Strumberger E 1998 Contributions to Plasma Physics **38** 106–111 (*Preprint* https://onlinelibrary.wiley.com/doi/pdf/10.1002/ctpp.2150380115) https://onlinelibrary.wiley.com/doi/abs/10.1002/ctpp.2150380115

[35] Lotz W, Nührenberg J and Schwab C 1990 Optimization, mhd mode and alpha particle confinement behaviour of HELIAS equilibria 13th IAEA Fusion Energy Conference (1 – 6 October 1990, Washington, USA) pp 603–611. 603–611 iAEA-CN-53/C-IH-S https://inis.iaea.org/collection/NCLCollectionStore/_Public/22/082/22082081.pdf

[36] Grieger G, Beidler C, Harmeyer E, Lotz W, Kißlinger J, Merkel P, Nührenberg J, Rau F, Strumberger E and Wobig H 1992 Fusion Technology **21** 1767–1778 (*Preprint* https://doi.org/10.13182/FST92-A29977) https://doi.org/10.13182/FST92-A29977

[37] Grieger G, Lotz W, Merkel P, Nührenberg J, Sapper J, Strumberger E, Wobig H, Burhenn R, Erckmann V, Gasparino U, Giannone L, Hartfuss H J, Jaenicke R, Kühner G, Ringler H, Weller A, Wagner F and W7-X Team and W7-AS Team 1992 Physics of Fluids B: Plasma Physics **4** 2081–2091 http://link.aip.org/link/?PFB/4/2081/1

[38] Andreeva T, Kisslinger J and Wobig H 2002 Characteristics of main configurations of Wendelstein 7-X Problems of Atomic Science and Technology Series: Plasma Physics vol 4 (Kharkov: National Science Center, Kharkov Institute of Physics and Technology) pp 45–47 http://vant.kipt.kharkov.ua/ARTICLE/VANT_2002_4/article_2002_4_45.pdf

[39] Geiger J, Beidler C D, Feng Y, Maaßberg H, Marushchenko N B and Turkin Y 2015 Plasma Physics and Controlled Fusion **57** 014004 http://stacks.iop.org/0741-3335/57/i=1/a=014004

[40] Bozhenkov S, Lazerson S, Otte M, Gates D, Pedersen T S and Wolf R 2016 Nuclear Fusion **56** 076002 http://stacks.iop.org/0029-5515/56/i=7/a=076002

[41] McNeely P, Barlak M, Baldzuhn J, Bozhenkov S, Drevlak M, Gawlik G, Heinemann B, Holtum D, Jagielski J, Kairys R, Nocentini R, Riedl R, Rong P, Rust N, Schroeder R, Speth E, Stbler A, Turos A and Wolf R 2013 Fusion Engineering and Design **88** 1034 – 1037 ISSN 0920-3796 proceedings of the 27th Symposium On Fusion Technology (SOFT-27); Lige, Belgium, September 24-28, 2012 http://www.sciencedirect.com/science/article/pii/S0920379613003001

[42] Rust N, Ford O P, Hartmann D, Heinemann B, McNeely P, Spanier A and Wolf R C 2019 Neutral beam injection on Wendelstein 7-X: beam transmission, shine through and effect of plasma current 46th EPS Conference on Plasma Physics (8–12 July 2019, Milan, Italy) p P5.1057 http://ocs.ciemat.es/EPS2019ABS/pdf/P5.1057.pdf

[43] Kißlinger J, Beidler C D, Harmeyer E, Rau F, Renner H and Wobig H 1994 Island divertor for the stellarator Wendelstein 7-X Controlled Fusion and Plasma Physisc, Proceedings of 21st European Conference, Montpellier, 1994 vol 18B, part 1 (European Physical Society, Geneva) pp 368 – 371

[44] Greuner H, Bitter W, Kerl F, Kißlinger J and Renner H 1995 Structure of divertor for the optimized

stellarator W7-X Fusion Technology, Proceedings of 18th Symposium Karlsruhe, 1994 vol 1 (Elsevier, Amsterdam and New-York) pp 323 – 326

[45] Zhang D, König R, Feng Y, Burhenn R, Brezinsek S, Jakubowski M, Buttenschön B, Niemann H, Pavone A, Krychowiak M, Kwak S, Svensson J, Gao Y, Pedersen T S, Alonso A, Baldzuhn J, Beidler C D, Biedermann C, Bozhenkov S, Brunner K J, Damm H, Hirsch M, Giannone L, Drewelow P, Effenberg F, Fuchert G, Hammond K C, Höfel U, Killer C, Knauer J, Laqua H P, Laube R, Pablant N, Pasch E, Penzel F, Rahbarnia K, Reimold F, Thomsen H, Winters V, Wagner F, Klinger T and team W X 2019 Phys. Rev. Lett. **123**(2) 025002 https://link.aps.org/doi/10.1103/PhysRevLett.123.025002

[46] Schmitz O, Jakubowski M, Koenig R, Krychowiak M, Reimold F, Anda G, Barbui T, Biedermann C, Bozhenkov S, Brezinsek S, Drewelow P, Effenberg F, Ennis D A, Feng Y, Flom E, Frerichs H, Ford O, Fuchert G, Gao Y, Gradic D, Hammond K C, Knauer J, Kornejew P, Kocsis G, Kremeyer T, Niemann H, Otte M, Pasch E, Perseo V, Schlisio G, Pedersen T S, Szepesi T, Wenzel U, Winters V, Wurden G A, Zhang D and Zoletnik S 2019 First-time realization of a stably detached, efficient-particle-exhaust divertor regime in the island divertor at Wendelstein 7-X 46th EPS Conference on Plasma Physics (8–12 July 2019, Milan, Italy) p I3.101 http://ocs.ciemat.es/EPS2019ABS/pdf/I3.101.pdf

[47] Andreeva T, Bräuer T, Bykov V, Egorov K, Endler M, Fellinger J, Kißlinger J, Köppen M and Schauer F 2015 Nuclear Fusion **55** 063025 http://stacks.iop.org/0029-5515/55/i=6/a=063025

[48] Bozhenkov S, Otte M, Biedermann C, Jakubowski M, Lazerson S, Pedersen T S and and R W 2018 Nuclear Fusion **59** 026004 https://doi.org/10.1088%2F1741-4326%2Faaf20c

[49] Lazerson S A, Bozhenkov S, Israeli B, Otte M, Niemann H, Bykov V, Endler M, Andreeva T, Ali A, Drewelow P, Jakubowski M, Sitjes A P, Pisano F and and B C 2018 Plasma Physics and Controlled Fusion **60** 124002 https://doi.org/10.1088%2F1361-6587%2Faae96b

[50] König R, Baldzuhn J, Biel W, Biedermann C, Bosch H, Bozhenkov S, Bräuer T, de Carvalho B B, Burhenn R, Buttenschön B, Cseh G, Czarnecka A, Endler M, Erckmann V, Estrada T, Geiger J, Grulke O, Hartmann D, Hathiramani D, Hirsch M, Jabłonski S, Jakubowski M, Kaczmarczyk J, Klinger T, Klose S, Kocsis G, Kornejew P, Krmer-Flecken A, Kremeyer T, Krychowiak M, Kubkowska M, Langenberg A, Laqua H P, Laux M, Liang Y, Lorenz A, Marchuk A, Moncada V, Neubauer O, Neuner U, Oosterbeek J, Otte M, Pablant N, Pasch E, Pedersen T, Rahbarnia K, Ryc L, Schmitz O, Schneider W, Schuhmacher H, Schweer B, Stange T, Thomsen H, Travere J M, Szepesi T, Wenzel U, Werner A, Wiegel B, Windisch T, Wolf R, Wurden G, Zhang D, Zimbal A and Zoletnik S 2015 Journal of Instrumentation **10** P10002–P10002 https://doi.org/10.1088%2F1748-0221%2F10%2F10%2Fp10002

[51] Knauer J, Kornejew P, Trimino Mora H, Hirsch M, Werner A and Wolf R 2016 A new dispersion interferometer for the stellarator Wendelstein 7-X 43rd EPS Conf. on Plasma Physics, Leuven, Belgium (2016), P4.017; http://ocs.ciemat.es/EPS2016PAP/pdf/P4.017.pdf

[52] Pasch E, Beurskens M N A, Bozhenkov S A, Fuchert G, Knauer J and Wolf R C 2016 Review of Scientific Instruments **87** 11E729 (*Preprint* http://aip.scitation.org/doi/pdf/10.1063/1.4962248) http://aip.scitation.org/doi/abs/10.1063/1.4962248

[53] Bozhenkov S, Beurskens M, Molin A D, Fuchert G, Pasch E, Stoneking M, Hirsch M, Höfel U, Knauer J, Svensson J, Mora H T and Wolf R 2017 Journal of Instrumentation **12** P10004 http://stacks.iop.org/1748-0221/12/i=10/a=P10004

[54] Hirsch, Matthias, Höfel, Udo, Oosterbeek, Johan Willem, Chaudhary, Neha, Geiger, Joachim, Hartfuss, Hans-Jürgen, Kasparek, Walter, Marushchenko, Nikolai, van Milligen, Boudewijn, Plaum, Burkhard, Stange, Torsten, Svensson, Jakob, Tsuchiya, Hayato, Wagner, Dietmar, McWeir, Gavin, Wolf, Robert and W7-X Team 2019 EPJ Web Conf. **203** 03007 https://doi.org/10.1051/epjconf/201920303007

[55] Hoefel U, Hirsch M, Kwak S, Pavone A, Svensson J, Stange T, Hartfuß H J, Schilling J, Weir G,

Oosterbeek J W, Bozhenkov S, Braune H, Brunner K J, Chaudhary N, Damm H, Fuchert G, Knauer J, Laqua H, Marsen S, Moseev D, Pasch E, Scott E R, Wilde F and Wolf R 2019 Review of Scientific Instruments **90** 043502 (*Preprint* https://doi.org/10.1063/1.5082542) https://doi.org/10.1063/1.5082542

[56] Pablant N A, Langenberg A, Alonso A, Beidler C D, Bitter M, Bozhenkov S, Burhenn R, Beurskens M, Delgado-Aparicio L, Dinklage A, Fuchert G, Gates D, Geiger J, Hill K W, Hfel U, Hirsch M, Knauer J, Krmer-Flecken A, Landreman M, Lazerson S, Maaberg H, Marchuk O, Massidda S, Neilson G H, Pasch E, Satake S, Svennson J, Traverso P, Turkin Y, Valson P, Velasco J L, Weir G, Windisch T, Wolf R C, Yokoyama M and Zhang D 2018 Physics of Plasmas **25** 022508 (*Preprint* https://doi.org/10.1063/1.4999842) https://doi.org/10.1063/1.4999842

[57] Langenberg A, Pablant N A, Wegner T, Traverso P, Marchuk O, Bruer T, Geiger B, Fuchert G, Bozhenkov S, Pasch E, Grulke O, Kunkel F, Killer C, Nicolai D, Satheeswaran G, Hollfeld K P, Schweer B, Krings T, Drews P, Offermanns G, Pavone A, Svensson J, Alonso J A, Burhenn R and Wolf R C 2018 Review of Scientific Instruments **89** 10G101 (*Preprint* https://doi.org/10.1063/1.5036536) https://doi.org/10.1063/1.5036536

[58] Ford O, Vano L, Alonso A, Baldzuhn J, Beurskens M, Biedermann C, Bozhenkov S, Fuchert G, Geiger B, Hartmann D, Jaspers R, Kappatou A, Langenberg A, Lazerson S, McDermott R, McNeely P, Neelis T, Pablant N, Pasch E, Rust N, Schroeder R, Scott E, Smith H, Wegner T, Kunkel F and Wolf R accepted in January 2020 Review of Scientific Instruments

[59] Rahbarnia K, Thomsen H, Neuner U, Schilling J, Geiger J, Fuchert G, Andreeva T, Endler M, Hathiramani D, Bluhm T, Zilker M, Carvalho B and and A W 2018 Nuclear Fusion **58** 096010 https://doi.org/10.1088%2F1741-4326%2Faacab0

[60] Zhang D, Burhenn R, Koenig R, Giannone L, Grodzki P A, Klein B, Grosser K, Baldzuhn J, Ewert K, Erckmann V, Hirsch M, Laqua H P and Oosterbeek J W 2010 Review of Scientific Instruments **81** 10E134 (*Preprint* https://doi.org/10.1063/1.3483194) https://doi.org/10.1063/1.3483194

[61] Pablant N A, Bell R E, Bitter M, Delgado-Aparicio L, Hill K W, Lazerson S and Morita S 2014 Review of Scientific Instruments **85** 11E424

[62] Langenberg A, Svensson J, Marchuk O, Fuchert G, Bozhenkov S, Damm H, Pasch E, Pavone A, Thomsen H, Pablant N A, Burhenn R and Wolf R C 2019 Review of Scientific Instruments **90** 063505 (*Preprint* https://doi.org/10.1063/1.5086283) https://doi.org/10.1063/1.5086283

[63] Hirshman S, van RIJ W and Merkel P 1986 Computer Physics Communications **43** 143 – 155 ISSN 0010-4655 http://www.sciencedirect.com/science/article/pii/0010465586900585

[64] Grahl M, Svensson J, Werner A, Andreeva T, Bozhenkov S, Drevlak M, Geiger J, Krychowiak M and Turkin Y 2018 IEEE Transactions on Plasma Science **46** 1114–1119 ISSN 0093-3813

[65] Andreeva T, Alonso J, Bozhenkov S, Brandt C, Endler M, Fuchert G, Geiger J, Grahl M, Klinger T, Krychowiak M, Langenberg A, Lazerson S, Neuner U, Rahbarnia K, Pablant N, Pavone A, Schilling J, Schmitt J, Thomsen H and Turkin Y 2019 Fusion Engineering and Design ISSN 0920-3796 http://www.sciencedirect.com/science/article/pii/S0920379618308159

[66] Fuchert G, Bozhenkov S, Pablant N, Rahbarnia K, Turkin Y, Alonso A, Andreeva T, Beidler C, Beurskens M, Dinklage A, Geiger J, Hirsch M, Hfel U, Knauer J, Langenberg A, Laqua H, Niemann H, Pasch E, Pedersen T S, Stange T, Svensson J, Mora H T, Wurden G, Zhang D and and R W 2018 Nuclear Fusion **58** 106029 https://doi.org/10.1088%2F1741-4326%2Faad78b

[67] Fuchert G, Dinklage A, Langenberg A, Beidler C, Zhang D, Pasch E, Warmer F, Damm H, Laqua H, Knauer J, Baldzuhn J, Brunner K J, Rahbarnia K, Hirsch M, Pablant N, Burhenn R, Wolf R, Lazerson S, Bozhenkov S, Pedersen T S, Stange T, Kazakov Y and Feng Y 2018 Increasing the density in W7-X: Benefits and limitations 27th IAEA Fusion Energy Conference (22 – 27 October 2018, Gandhinagar, India) https://conferences.iaea.org/indico/event/151/contributions/5833/

[68] Pavone A, Hergenhahn U, Krychowiak M, Hoefel U, Kwak S, Svensson J, Kornejew P, Winters V, Koenig R, Hirsch M, Brunner K J, Pasch E, Knauer J, Fuchert G, Scott E, Beurskens M,

Effenberg F, Zhang D, Ford O, Vanó L and Wolf R 2019 Journal of Instrumentation **14** C10003–C10003 https://doi.org/10.1088%2F1748-0221%2F14%2F10%2Fc10003

[69] Marushchenko, N B, Beidler, C D, Erckmann, V, Geiger, J, Helander, P, Laqua, HP, Maassberg, H and Turkin, Y 2012 EPJ Web of Conferences **32** 01004 https://doi.org/10.1051/epjconf/20123201004

[70] Marushchenko N, Turkin Y and Maassberg H 2014 Computer Physics Communications **185** 165 – 176 ISSN 0010-4655 http://www.sciencedirect.com/science/article/pii/S0010465513003032

[71] Wolf R, Ali A, Alonso A, Baldzuhn J, Beidler C, Beurskens M, Biedermann C, Bosch H S, Bozhenkov S, Brakel R, Dinklage A, Feng Y, Fuchert G, Geiger J, Grulke O, Helander P, Hirsch M, Höfel U, Jakubowski M, Knauer J, Kocsis G, König R, Kornejew P, Krämer-Flecken A, Krychowiak M, Landreman M, Langenberg A, Laqua H, Lazerson S, Maßberg H, Marsen S, Marushchenko M, Moseev D, Niemann H, Pablant N, Pasch E, Rahbarnia K, Schlisio G, Stange T, Pedersen T S, Svensson J, Szepesi T, Mora H T, Turkin Y, Wauters T, Weir G, Wenzel U, Windisch T, Wurden G, Zhang D, Abramovic I, Äkäslompolo S, Aleynikov P, Aleynikova K, Alzbutas R, Anda G, Andreeva T, Ascasibar E, Assmann J, Baek S G, Banduch M, Barbui T, Barlak M, Baumann K, Behr W, Benndorf A, Bertuch O, Biel W, Birus D, Blackwell B, Blanco E, Blatzheim M, Bluhm T, Böckenhoff D, Bolgert P, Borchardt M, Borsuk V, Boscary J, Böttger L G, Brand H, Brandt C, Bräuer T, Braune H, Brezinsek S, Brunner K J, Brünner B, Burhenn R, Buttenschön B, Bykov V, Calvo I, Cannas B, Cappa A, Carls A, Carraro L, Carvalho B, Castejon F, Charl A, Chernyshev F, Cianciosa M, Citarella R, Ciupiski , Claps G, Cole M, Cole M, Cordella F, Cseh G, Czarnecka A, Czermak A, Czerski K, Czerwinski M, Czymek G, da Molin A, da Silva A, Dammertz G, Danielson J, de la Pena A, Degenkolbe S, Denner P, Dhard D, Dostal M, Drevlak M, Drewelow P, Drews P, Dudek A, Dundulis G, Durodie F, van Eeten P, Effenberg F, Ehrke G, Endler M, Ennis D, Erckmann E, Esteban H, Estrada T, Fahrenkamp N, Feist J H, Fellinger J, Fernandes H, Fietz W, Figacz W, Fontdecaba J, Ford O, Fornal T, Frerichs H, Freund A, Führer M, Funaba T, Galkowski A, Gantenbein G, Gao Y, Regana J G, Garcia-Munoz M, Gates D, Gawlik G, Geiger B, Giannella V, Gierse N, Gogoleva A, Goncalves B, Goriaev A, Gradic D, Grahl M, Green J, Grosman A, Grote H, Gruca M, Guerard C, Haiduk L, Han X, Harberts F, Harris J, Hartfu H J, Hartmann D, Hathiramani D, Hein B, Heinemann B, Heitzenroeder P, Henneberg S, Hennig C, Sanchez J H, Hidalgo C, Hölbe H, Hollfeld K, Hölting A, Höschen D, Houry M, Howard J, Huang X, Huber M, Huber V, Hunger H, Ida K, Ilkei T, Illy S, Israeli B, Ivanov A, Jablonski S, Jagielski J, Jelonnek J, Jenzsch H, Junghans P, Kacmarczyk J, Kaliatka T, Kallmeyer J P, Kamionka U, Karalevicius R, Kasahara H, Kasparek W, Kenmochi N, Keunecke M, Khilchenko A, Kinna D, Kleiber R, Klinger T, Knaup M, Kobarg T, Köchl F, Kolesnichenko Y, Könies A, Köppenppen M, Koshurinov J, Koslowski R, Köster F, Koziol R, Krämer M, Krampitz R, Kraszewsk P, Krawczyk N, Kremeyer T, Krings T, Krom J, Krzesinski G, Ksiazek I, Kubkowska M, Kühnerhner G, Kurki-Suonio T, Kwak S, Lang R, Langish S, Laqua H, Laube R, Lechte C, Lennartz M, Leonhardt W, Lewerentz L, Liang Y, Linsmeier C, Liu S, Lobsien J F, Loesser D, Cisquella J L, Lore J, Lorenz A, Losert M, Lubyako L, Lcke A, Lumsdaine A, Lutsenko V, Majano-Brown J, Marchuk O, Mardenfeld M, Marek P, Massidda S, Masuzaki S, Maurer D, McCarthy K, McNeely P, Meier A, Mellein D, Mendelevitch B, Mertens P, Mikkelsen D, Mishchenko O, Missal B, Mittelstaedt J, Mizuuchi T, Mollen A, Moncada V, Mönnich T, Morizaki T, Munk R, Murakami S, Musielok F, Nafradi G, Nagel M, Naujoks D, Neilson H, Neubauer O, Neuner U, Ngo T, Nocentini R, Nührenberg C, Nührenberg J, Obermayer S, Offermanns G, Ogawa K, Ongena J, Oosterbeek J, Orozco G, Otte M, Rodriguez L P, Pan W, Panadero N, Alvarez N P, Panin A, Papenfuß D, Paqay S, Pavone A, Pawelec E, Pelka G, Peng X, Perseo V, Peterson B, Pieper A, Pilopp D, Pingel S, Pisano F, Plaum B, Plunk G, Povilaitis M, Preinhaelter J, Proll J, Puiatti M E, Sitjes A P, Purps F, Rack M, Recsei S, Reiman A, Reiter D, Remppel F, Renard S, Riedl R, Riemann J, Rimkevicius S, Riße K, Rodatos A, Röhlinger H, Rom M, Rong P, Roscher H J, Roth B, Rudischhauser L, Rummel

K, Rummel T, Runov A, Rust N, Ryc L, Ryosuke S, Sakamoto R, Samartsev A, Sanchez M, Sano F, Satake S, Satheeswaran G, Schacht J, Schauer F, Scherer T, Schlaich A, Schlüter K H, Schmitt J, Schmitz H, Schmitz O, Schmuck S, Schneider M, Schneider W, Scholz M, Scholz P, Schrittwieser R, Schröder M, Schröder T, Schroeder R, Schumacher H, Schweer B, Shanahan B, Shikhovtsev I, Sibilia M, Sinha P, Sipli S, Skodzik J, Slaby C, Smith H, Spiess W, Spong D, Spring A, Stadler R, Standley B, Stephey L, Stoneking M, Stridde U, Sulek Z, Surko C, Suzuki Y, Szabo V, Szabolics T, Szökefalvi-Nagy Z, Tamura N, Terra A, Terry J, Thomas J, Thomsen H, Thumm M, von Thun C, Timmermann D, Titus P, Toi K, Travere J, Traverso P, Tretter J, Tsuchiya H, Tsujimura T, Tulipan S, Turnyanskiy M, Unterberg B, Urban J, Urbonavicius E, Vakulchyk I, Valet S, van Millingen B, Vela L, Velasco J L, Vergote M, Vervier M, Vianello N, Viebke H, Vilbrandt R, Vorkörper A, Wadle S, Wagner F, Wang E, Wang N, Warmer F, Wegener L, Weggen J, Wei Y, Wendorf J, Werner A, Wiegel B, Wilde F, Winkler E, Winters V, Wolf S, Wolowski J, Wright A, Xanthopoulos P, Yamada H, Yamada I, Yasuhara R, Yokoyama M, Zajac J, Zarnstorff M, Zeitler A, Zhang H, Zhu J, Zilker M, Zimbal A, Zocco A, Zoletnik S and Zuin M 2017 Nuclear Fusion **57** 102020 http://stacks.iop.org/0029-5515/57/i=10/a=102020

[72] Bozhenkov S, Baldzuhn J, Kazakov Y, Laqua H, Alonso J, Brandt C, Brunner K, Damm H, Fuchert G, Hirsch M, Hfel U, Jakubowski M, Knauer J, Kocsis G, Knig R, Langenberg A, Lazerson S, Marushchenko N, McCarthy K, Pasch E, Pablant N, Panadero Alvarez N, Rahbarnia K, Schmitt J, Thomsen H, Turkin Y, Warmer F, Wurden G, Zhang D, Pedersen T and Wolf R 2018 High density and high performance operation with pellet injection in W7-X 27th IAEA Fusion Energy Conference (22 – 27 October 2018, Gandhinagar, India) https://conferences.iaea.org/indico/event/151/contributions/5948/

[73] Brandt C, Broszat T, Thomsen H, Laube R, Marquardt M, Franz P, Schlke M, Sieber T and Weiflog S 2017 Fusion Engineering and Design **123** 887 – 891 ISSN 0920-3796 proceedings of the 29th Symposium on Fusion Technology (SOFT-29) Prague, Czech Republic, September 5-9, 2016 http://www.sciencedirect.com/science/article/pii/S092037961730323X

[74] Brandt C, Schilling J, Thomsen H, Broszat T, Laube R, Schrder T, Andreeva T, Beurskens M, Bozhenkov S, Brunner K, Card A, Cordes C, Damm H, Fuchert G, Gallowski K, Gutzmann R, Knauer J, Laqua H, Marquardt M, Nelde P, Neuner U, Pasch E, Rahbarnia K, Recknagel J, Schlke M, Scott E R and Sieber T 2019 accepted to Plasma Physics and Controlled Fusion

[75] Stange, Torsten, Laqua, Heinrich Peter, Beurskens, Marc, Bosch, Hans-Stephan, Bozhenkov, Sergey, Brakel, Rudolf, Braune, Harald, Brunner, Kai Jakob, Cappa, Alvaro, Dinklage, Andreas, Erckmann, Volker, Fuchert, Golo, Gantenbein, Gerd, Gellert, Florian, Grulke, Olaf, Hartmann, Dirk, Hirsch, Matthias, Höfel, Udo, Kasparek, Walter, Knauer, Jens, Langenberg, Andreas, Marsen, Stefan, Marushchenko, Nikolai, Moseev, Dmitry, Pablant, Novomir, Pasch, Ekkehard, Rahbarnia, Kian, Mora, Humberto Trimino, Tsujimura, Toru, Turkin, Yuriy, Wauters, Tom and Wolf, Robert 2017 EPJ Web Conf. **157** 02008 https://doi.org/10.1051/epjconf/201715702008

[76] Edlund E M, Porkolab M, Huang Z, Grulke O, Bttger L G, von Sehren C and von Stechow A 2018 Review of Scientific Instruments **89** 10E105 (*Preprint* https://doi.org/10.1063/1.5038804) https://doi.org/10.1063/1.5038804

[77] Stroth U 2005 Transport in Toroidal Plasmas (Berlin, Heidelberg: Springer Berlin Heidelberg) pp 213–267 ISBN 978-3-540-31521-6 https://doi.org/10.1007/11360360_9

[78] Hirshman S P, Shaing K C, van Rij W I, Beasley C O and Crume E C 1986 The Physics of Fluids **29** 2951–2959 (*Preprint* https://aip.scitation.org/doi/pdf/10.1063/1.865495) https://aip.scitation.org/doi/abs/10.1063/1.865495

[79] van Rij W I and Hirshman S P 1989 Physics of Fluids B: Plasma Physics **1** 563–569 (*Preprint* https://doi.org/10.1063/1.859116) https://doi.org/10.1063/1.859116

[80] Pablant N, Langenberg A, Alonso J, Baldzuhn J, Beidler C, Bozhenkov S, Burhenn R, Brunner K, Dinklage A, Fuchert G, Ford O, Gates D, Geiger J, Hirsch M, Hfel U, Kazakov Y, Knauer J, Krychowiak M, Laqua H, Landreman M, Lazerson S, Maaberg H, Marchuk O, Mollén A, Pasch

E, Pavone A, Satake S, Schrder T, Smith H, Svensson J, Traverso P, Turkin Y, Velasco J, von Stechow A, Warmer F, Weir G, Wolf R and Zhang D 2019 submitted to Nuclear Fusion

[81] Turkin Y, Beidler C D, Maaberg H, Murakami S, Tribaldos V and Wakasa A 2011 Physics of Plasmas **18** 022505 (*Preprint* https://doi.org/10.1063/1.3553025) https://doi.org/10.1063/1.3553025

[82] Turkin Y, Maassberg H, Beidler C D, Geiger J and Marushchenko N B 2006 Fusion Science and Technology **50** 387–394 (*Preprint* https://doi.org/10.13182/FST06-5) https://doi.org/10.13182/FST06-5

[83] Dinklage A, Beidler C, Helander P and et al 2018 Nature Physics **14** 855–860

[84] Romanelli F 1989 Plasma Physics and Controlled Fusion **31** 1535–1549 https://doi.org/10.1088%2F0741-3335%2F31%2F10%2F005

[85] Helander P, Bird T, Jenko F, Kleiber R, Plunk G, Proll J, Riemann J and Xanthopoulos P 2015 Nuclear Fusion **55** 053030 https://doi.org/10.1088%2F0029-5515%2F55%2F5%2F053030

[86] Alcusón J A, Xanthopoulos P, Plunk G G, Helander P, Wilms F, Turkin Y, von Stechow A and Grulke O 2020 Plasma Physics and Controlled Fusion **62** 035005 https://doi.org/10.1088%2F1361-6587%2Fab630e

[87] von Stechow A, Huang Z, Bttger L G, Edlund E, Porkolab M, Windisch T, Weir G, Alcuson J, Xanthopoulos P, Wegner T, Geiger B, Bussiahn R and Grulke O 2019 Density turbulence modification by gradient control in W7-X 46th EPS Conference on Plasma Physics (8–12 July 2019, Milan, Italy) p P5.1097 http://ocs.ciemat.es/EPS2019ABS/pdf/P5.1097.pdf

[88] McCormick K, Grigull P, Burhenn R, Brakel R, Ehmler H, Feng Y, Gadelmeier F, Giannone L, Hildebrandt D, Hirsch M, Jaenicke R, Kisslinger J, Klinger T, Klose S, Knauer J P, König R, Kühner G, Laqua H P, Naujoks D, Niedermeyer H, Pasch E, Ramasubramanian N, Rust N, Sardei F, Wagner F, Weller A, Wenzel U and Werner A 2002 Phys. Rev. Lett. **89**(1) 015001 https://link.aps.org/doi/10.1103/PhysRevLett.89.015001